minerals

MDPI

Article

The Influence of Seasonal Variations in a Continental Lacustrine Basin in an Arid Climate on the Occurrence Characteristics of Gypsum: A Case Study from the Paleogene Bottom Sandstone Member, Tabei Uplift

Xiaoyang Gao [1], Wenxiang He [1], Luxing Dou [1,*], Jingwen Yan [2], Qi Sun [2], Zhenli Yi [2] and Bin Li [2]

[1] College of Resources and Environment, Yangtze University, Wuhan 430100, China; 2021730044@yangtzeu.edu.cn (X.G.); hwx@yangtzeu.edu.cn (W.H.)
[2] Research Institute of Exploration and Development, Tarim Oilfield Company, CNPC, Korla 841000, China; yanjw-tlm@petrochina.com.cn (J.Y.); m13596956922@163.com (Q.S.); 18801041050@163.com (Z.Y.); 705442443@139.com (B.L.)
* Correspondence: douluxing@hotmail.com

Abstract: The occurrence of gypsum in clastic rocks of continental saline lake basins reflects complex depositional and diagenetic processes. However, its genesis remains relatively understudied. Based on core descriptions and thin-section analyses, this study investigates the occurrence types and genetic mechanisms of gypsum in the Bottom Sandstone Member of the northern Tabei Uplift. Five types of gypsum occurrences are identified: layered gypsum, gypsum clasts, spotted gypsum, gypsum nodules, and a mixed deposition of clastic rocks and gypsum. The mixed deposition of clastic rocks and gypsum includes gypsiferous mudstone, muddy gypsum, gypsiferous mudstone containing muddy clasts, and sandy gypsum. Layered gypsum, spotted gypsum, gypsiferous mudstone, and muddy gypsum mainly result from in situ chemical precipitation during periods of high evaporation and reduced runoff. In contrast, gypsum clasts, gypsiferous mudstone containing muddy clasts, and sandy gypsum reflect processes of transportation and reworking induced by flood events. Seasonal variations in hydrodynamic conditions play a critical role in the formation and distribution of gypsum. During dry periods, surface runoff weakens or ceases, and the salinity of lake water or pore water in clastic deposits increases due to intense evaporation, promoting gypsum precipitation. During flood periods, increased runoff can erode previously formed gypsum, which is subsequently transported and deposited as gypsum clasts. The morphology of gypsum varies with its transport distance. These findings enhance our understanding of clastic–evaporite mixed systems in arid continental lacustrine settings and provide insights into sedimentary processes influenced by seasonal climatic fluctuations.

Keywords: gypsum; salt lake–delta; seasonal change; sedimentary process

check for updates

Academic Editors: Santanu Banerjee, Xiaomin Zhu, Qianghu Liu, Hehe Chen, Mingxuan Tan and Hongtao Zhu

Received: 2 May 2025
Revised: 5 June 2025
Accepted: 10 June 2025
Published: 12 June 2025

Citation: Gao, X.; He, W.; Dou, L.; Yan, J.; Sun, Q.; Yi, Z.; Li, B. The Influence of Seasonal Variations in a Continental Lacustrine Basin in an Arid Climate on the Occurrence Characteristics of Gypsum: A Case Study from the Paleogene Bottom Sandstone Member, Tabei Uplift. *Minerals* **2025**, *15*, 639. https://doi.org/10.3390/min15060639

Copyright: © 2025 by the authors. Licensee MDPI, Basel, Switzerland. This article is an open access article distributed under the terms and conditions of the Creative Commons Attribution (CC BY) license (https://creativecommons.org/licenses/by/4.0/).

1. Introduction

Gypsum is a distinctive sedimentary mineral formed under intense evaporative conditions, commonly occurring in a variety of geological settings shaped by both sedimentary and diagenetic processes, particularly in arid to semi-arid environments [1–3]. These gypsum deposits occur in various forms, including thick massive beds, thin interlayers with other lithologies, or as dispersed single crystals, cement, or nodules within different host rocks [4–6]. In general, the formation of gypsum is closely associated with evaporative

processes. Different occurrence modes of gypsum reflect distinct depositional environments and physicochemical conditions. Investigating the genesis of these gypsum types is of great significance for reconstructing paleoclimatic conditions, hydrodynamic settings, and the evolution of sedimentary facies during ancient depositional periods [5,7,8].

Many researchers have suggested that gypsum typically forms in depositional environments characterized by high evaporation rates under arid to semi-arid climatic conditions [9]. Two main types of depositional settings are commonly identified: (1) relatively enclosed water bodies, where evaporation leads to the development of brine stratification and the precipitation of sulfate minerals on the basin floor [2,8,10], and (2) extremely shallow water environments such as mudflats, dry salt lakes, and tidal flats, where brines form through intense evaporation and gypsum precipitates in various forms within the host rocks [1,4,5]. In addition to evaporative processes, non-evaporative mechanisms have also been proposed for the formation of gypsum, including diagenesis [9,11,12], hydrothermal activity [13], and biological processes [14,15]. It is worth noting that the formation of these sulfate minerals generally falls within the category of chemical precipitation. However, in nature, gypsum also exists within clastic rocks, which results from mechanical transport rather than chemical deposition [3,16,17]. In arid or semi-arid continental basins, in addition to aeolian transport, mechanical processes such as fluvial and wave activity are typically regulated by seasonal climatic variations. These processes not only directly or repeatedly transport and redistribute clastic materials and evaporite salts but also influence the spatial and temporal distribution of salinity by controlling the concentration and dilution of lake water [8,14,16,18]. Mechanical transport and evaporative concentration processes often operate alternately or synergistically, facilitating the formation and preservation of gypsum in diverse occurrence modes under varying hydrodynamic conditions. Research on the various occurrence modes of gypsum formed through hydrodynamic reworking is still limited, and the understanding of its controlling mechanisms remains insufficient.

The Cretaceous to Paleogene period was a globally significant greenhouse climate era [19–21]. During this time, the Tarim Basin experienced an arid to semi-arid paleoclimate [22–24], which led to the deposition of thick red clastic rocks and evaporite deposits [25,26]. The collision of the Indian and Eurasian plates during the Paleogene Kumugeliemu Group deposition triggered a Tethyan marine transgression [27–29], delivering abundant moisture to the northern Tarim Basin. The interaction between increased moisture input and the prevailing arid climate led to the formation of a continental saline lake. Sustained evaporation facilitated the development of a sedimentary system characterized by the coexistence of clastic rocks and evaporite deposits [30,31]. Seasonal climatic variations further regulated the sedimentary environment, causing gypsum to exhibit various occurrence modes at different stages. This provides a solid foundation for the in-depth exploration of the coexistence mechanism and sedimentary processes of clastic rocks and evaporites. This study summarizes the occurrence characteristics of gypsum in the research area through core observation and thin-section analysis, explores its genesis mechanisms, and identifies the controlling factors in its formation process. Based on this, this study further investigates how seasonal climatic variations influence the formation process and spatial distribution characteristics of gypsum and establishes depositional models for different types of gypsum.

2. Geological Setting

The Tarim Basin, located in the southern part of the Xinjiang Uygur Autonomous Region in Northwestern China, is the largest inland basin in the country and also the most prolific sedimentary basin in terms of hydrocarbon resources [32]. Bounded by the Tianshan Mountains to the north, the Kunlun Mountains to the south, and the Altun

Mountains to the southeast (Figure 1A), the basin extends approximately 520 km from north to south at its widest point and about 1400 km from east to west, covering an area of approximately 560,000 km^2. The basin's elevation ranges from 800 to 1300 m above sea level, with a general topographic gradient descending from west to east. The Tarim Basin is composed of seven tectonic units, among which the Tabei Uplift is situated in the northern part (Figure 1B). It exhibits an overall east–west orientation and belongs to the cratonic domain within the basin. This pre-Jurassic paleo-uplift is buried beneath the southern slope of the Kuqa Cenozoic foreland basin. It extends approximately 480 km from east to west and 70 to 100 km from north to south, with a general westward dip [33,34]. Compared with the adjacent depression zones, the Tabei Uplift has undergone strong and sustained tectonic activity, as evidenced by the development of multiple prominent unconformities, intense uplift and erosion, and complex fault-related deformation [35,36]. The Tabei Uplift is typically subdivided into several secondary structural units, including the Wensu Bulge, Yingmaili Low Uplift, Luntai Bulge, and Lunnan Low Uplift [25]. This study focuses on the western part of the Tabei Uplift, with particular emphasis on the Yangtak Tectonic Belt, the Karayuergun Tectonic Belt, the WM7 Fault Zone, and the intervening areas (Figure 1C).

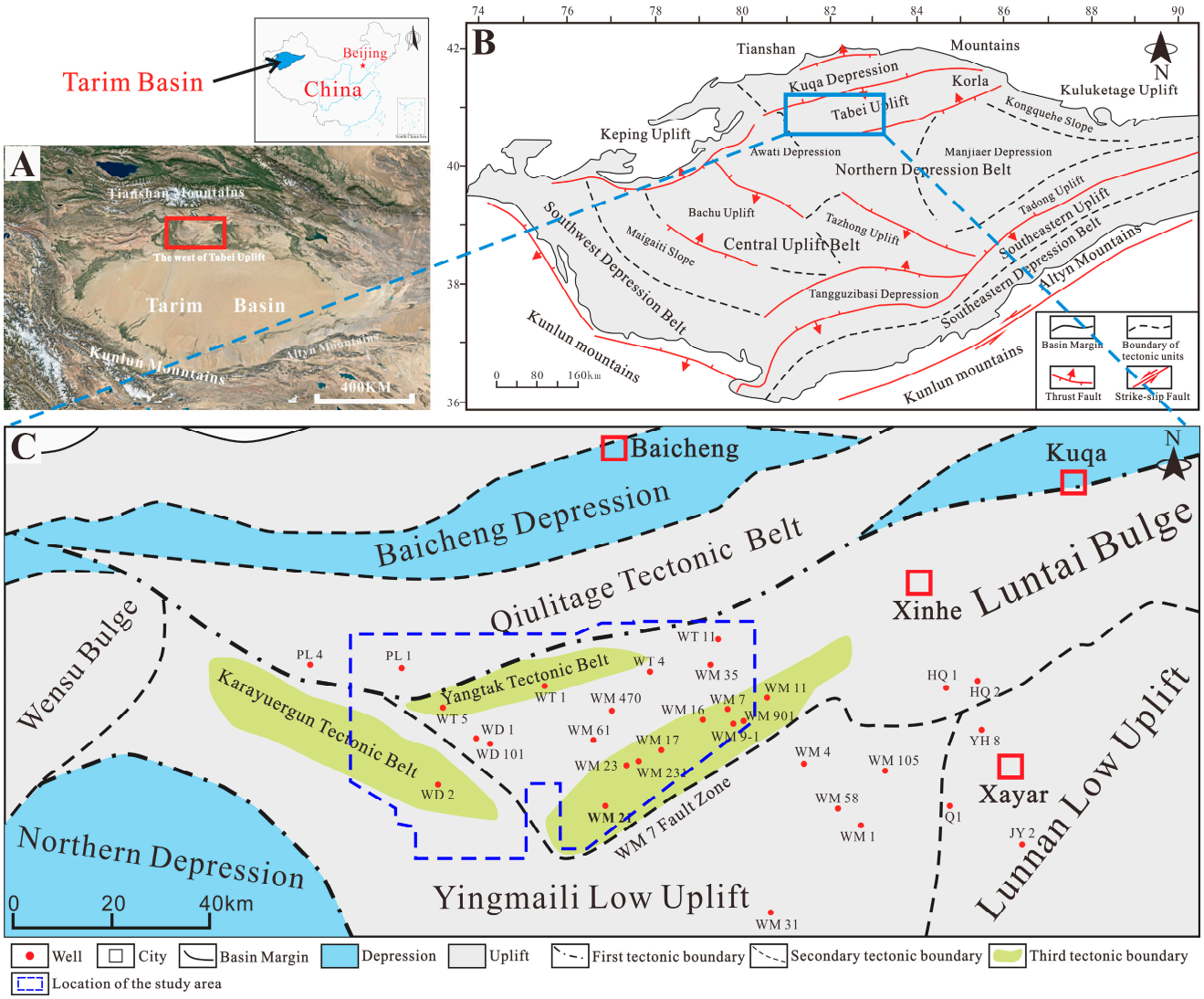


Figure 1. Location map of the study area. (**A**) Satellite photos of the Tarim Basin. (**B**) Schematic diagram of the structure of the Tarim Basin. The blue box shows the position of the western part of the Tabei uplift. (**C**) Structural unit map of the western part of the Tabei Uplift.

The Paleogene strata in the study area include the Suweiyi Formation and the Kumugeliemu Group. According to regional stratigraphic correlation, the Kumugeliemu Group in the Tabei uplift is inferred to have been deposited during the Paleocene to early Eocene [37,38]. The Kumugeliemu Group, in ascending order, consists of the Bottom Sandstone Member, Lower Gypsum Mudstone Member, Gypsum-Salt Member, and Upper Gypsum Mudstone Member. Among these, the Bottom Sandstone Member is in angular unconformable contact with the underlying Cretaceous Bashijiqike Formation. In the Tabei Uplift, the Bottom Sandstone Member is predominantly characterized by a saline lake–deltaic depositional system [39,40]. Based on lithological variations, this interval can be subdivided, in ascending order, into a Lowstand Systems Tract (LST), a Transgressive Systems Tract (TST), and a Highstand Systems Tract (HST). The LST is dominated by sandstones and primarily represents a deltaic depositional environment. The TST is characterized by mudstone and gypsiferous mudstone deposits, which are regionally continuous; thin layers of siltstone and fine sandstone occur at the base, indicating a delta–lacustrine transitional environment. The HST is mainly composed of grayish-white gypsum and gray dolostone, with widespread distribution, and reflects an overall lacustrine depositional setting (Figure 2) [30]. This study focuses on the LST–TST interval of the Paleogene Bottom Sandstone Member, which is mainly composed of interbedded brownish red sandstones and mudstones, with gypsum developed within the clastic deposits (Figure 2).

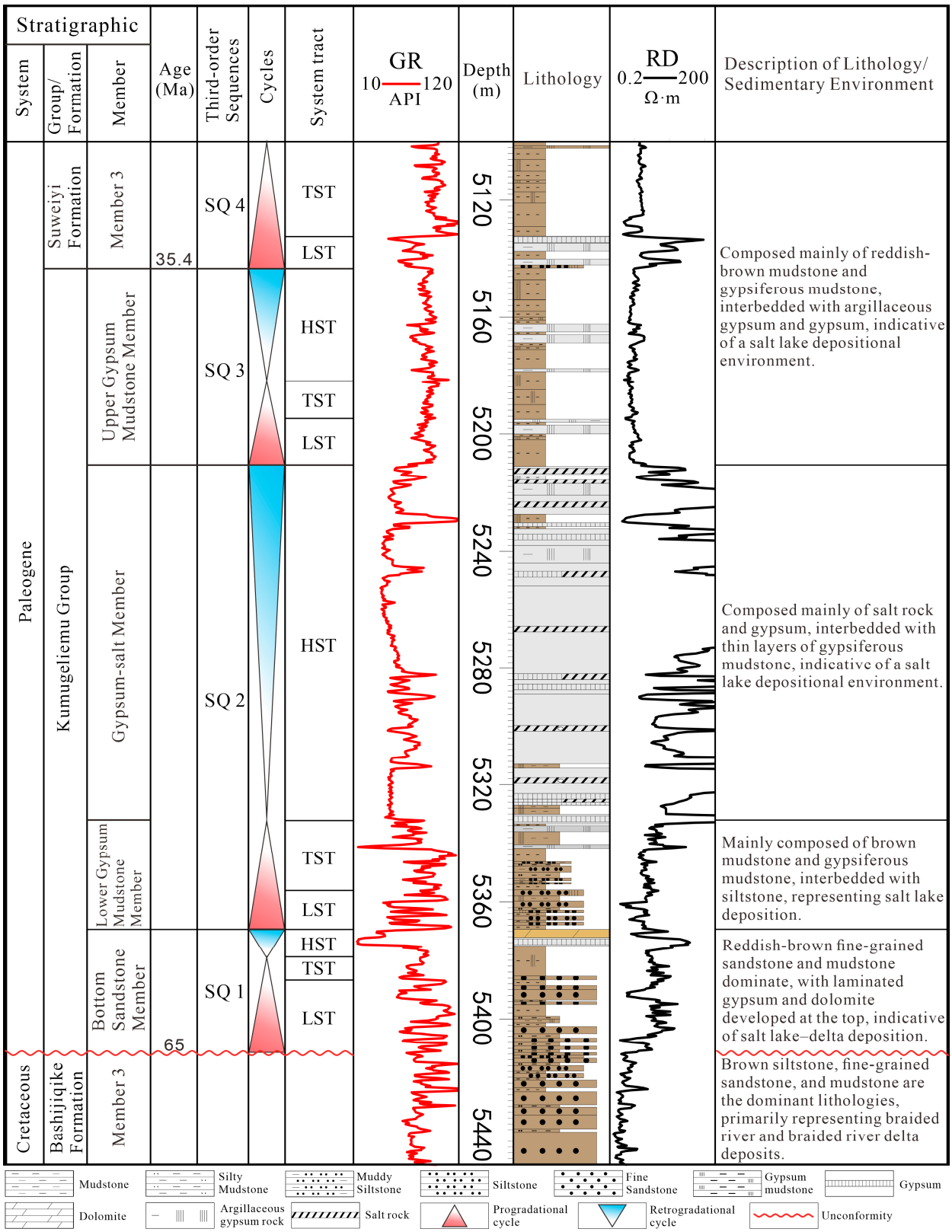


Figure 2. Development characteristics of the Paleogene strata at well WT502 in the western Tabei Uplift. GR represents the gamma ray log, while RD represents the resistivity log. In Paleogene strata, sandstone typically shows low GR and RD values; mudstone exhibits high GR values, and its RD values are relatively complex due to compositional differences; halite and gypsum are characterized by very low GR values and very high RD values.

3. Dataset and Methodology

This study examined nearly 80 m of core, providing detailed descriptions and collecting photographs. Additionally, well log curves and logging data from 60 wells were collected to identify the lithology and sedimentary facies in wells without core samples. This study used thin sections for gypsum petrography. The thin sections were provided by the Tarim Oilfield, and the samples were examined under orthogonal polarization.

Nineteen lithofacies types were identified through core observations (Table 1). The lithofacies classification scheme follows a modified version of Miall (1988) [41]. The depositional environment of the study area was analyzed using the development characteristics of the lithofacies. Core and thin-section analyses were applied to investigate the occurrence and features of gypsum. The formation of gypsum was investigated via sedimentary facies analysis, and a conceptual model of its distribution was established. Furthermore, this study examines the influence of seasonal variations on salt lake–delta sedimentary processes under arid climatic conditions, providing a scientific framework for understanding the formation of clastic–evaporite mixed sediments in continental lake basins.

Table 1. Facies classification and interpretation of the base sandstone member in the study area.

Code	Lithology	Sedimentary Structure	Sedimentary Interpretation
Mm	Gray-green and brown-red mudstone, silty mudstone	Massive structure, gypsum nodules.	A stable hydrodynamic environment with relatively poor drainage conditions [42], gradually leading to the formation of gypsum nodules as evaporation proceeds [43].
Mmc	Brown-red mudstone, silty mudstone	Massive structure, dry cracking phenomenon.	An exposed environment with relatively poor drainage conditions, where the surface of the sediment undergoes shrinkage due to water loss during evaporation [44].
Mgc	Gray-green and brown-red mudstone	Developed gypsum nodules and mud clasts.	Hydrodynamic conditions are weak, but wave and flood events frequently cause gypsum fragmentation and transport, often accompanied by small mud clasts [45].
Mh	Gray-green, brown-red mudstone, silty mudstone	Horizontal bedding, biogenic disturbance structures.	Fine-grained sediments result from vertical accretion in a still-water environment, with biological activity potentially disrupting the original sedimentary structures [46].
Mw	Gray-green, brown-red mudstone, silty mudstone	Asymmetric wavy bedding.	Formed by the forward motion of unidirectional flow [47].
MG	Gray-green gypsiferous mudstone, muddy gypsum	Gypsum and mudstone are mixed in the sediment, with no distinct boundary between them.	In a weak hydrodynamic environment, terrigenous fine-grained materials are transported to the depositional area, where they deposit alongside gypsum formed by salt lake evaporation [48].
Msb	Gray-green, brown-red mudstone, silty mudstone	Sandy bands.	Under stable hydrodynamic conditions, river and wave influence brought in small amounts of sandy sediments [49].
Gm	White gypsum	Massive structure with layered gypsum distribution; may also display features such as dry cracking and network patterns.	In closed or semi-closed water bodies, intense evaporation leads to calcium sulfate supersaturation and crystallization [50].

Table 1. *Cont.*

Code	Lithology	Sedimentary Structure	Sedimentary Interpretation
Mgs	Gray-green, brown-red mudstone	Spotted gypsum.	Often formed during the unconsolidated stage, gypsum crystals are formed in mud-rich sediments through evaporation and crystallization of pore water rich in Ca^{2} extsupscript+ and SO extsubscript4^{2-} [6].
Sgs	Brown fine-grained sandstone	Spotted gypsum.	Formed through evaporation and crystallization of brine in the pores [6].
Sm	Brown fine-grained sandstone	Massive structure.	Sediments undergo rapid deposition in the high-flow regime of upstream fluids [51].
Se	Brown fine-grained sandstone	Erosional base; lag deposit, rip-up mud clast, muddy clasts, or gypsum lumps.	During flood events, mudstone or gypsum deposits undergo reworking, transforming into lag deposits at the base of the distributary channels [52].
Sp	Brown, grayish-green fine-grained sandstone	Parallel lamination.	Formed by flowing water under high-energy hydrodynamic conditions [53].
Sc	Brown, grayish-green fine-grained sandstone.	Trough cross-bedding; planar cross-bedding.	Migration of sand bar forms in distributary channels [54].
Sh	Brown fine sandstone	Hyperpycnal flow.	During flood events, hyperpycnal flows are triggered by turbid river water denser than ambient lake water [32].
Smb	Brown fine-grained sandstone	Muddy bands, bioturbation structures.	Formed by periodic changes in flow energy; during low-energy conditions, reduced sedimentation rates favor biological activity, which can disrupt the original sedimentary structures [55].
Sr	Brown, gray-green fine-grained sandstone.	Ripple cross-bedding.	Unidirectional ripple migration under low flow conditions [54].
Sw	Brown fine-grained sandstone	Wave-formed ripple cross-lamination.	It results from prolonged wave action and fluctuating hydrodynamic conditions [56].
Sg	Light beige sandy gypsum	Sandy clasts mixed with gypsum.	In a high-salinity water environment, under the influence of strong hydrodynamic transport, clastic materials and gypsum are deposited together [57,58].

4. Results

4.1. Sedimentary Facies Description and Interpretation

4.1.1. Delta Plain

Distributary Channel (FA1)

Description: FA1 primarily consists of brown, fine-grained, and poorly sorted sandstones. Multiple fining-upward sandstone units can be observed, though the grain size variations are relatively minor. The contact with the underlying mudstone is abrupt (Figure 3). Multiple mud clast-bearing erosional surfaces are observed within FA1 (Figure 3a,c,f,h), along with parallel lamination (Figure 3d), cross-bedding (Figure 3e), and massive structures (Figure 3b,g). The lithofacies of FA1 are primarily composed of Sm, Se, Sp, and Sc.

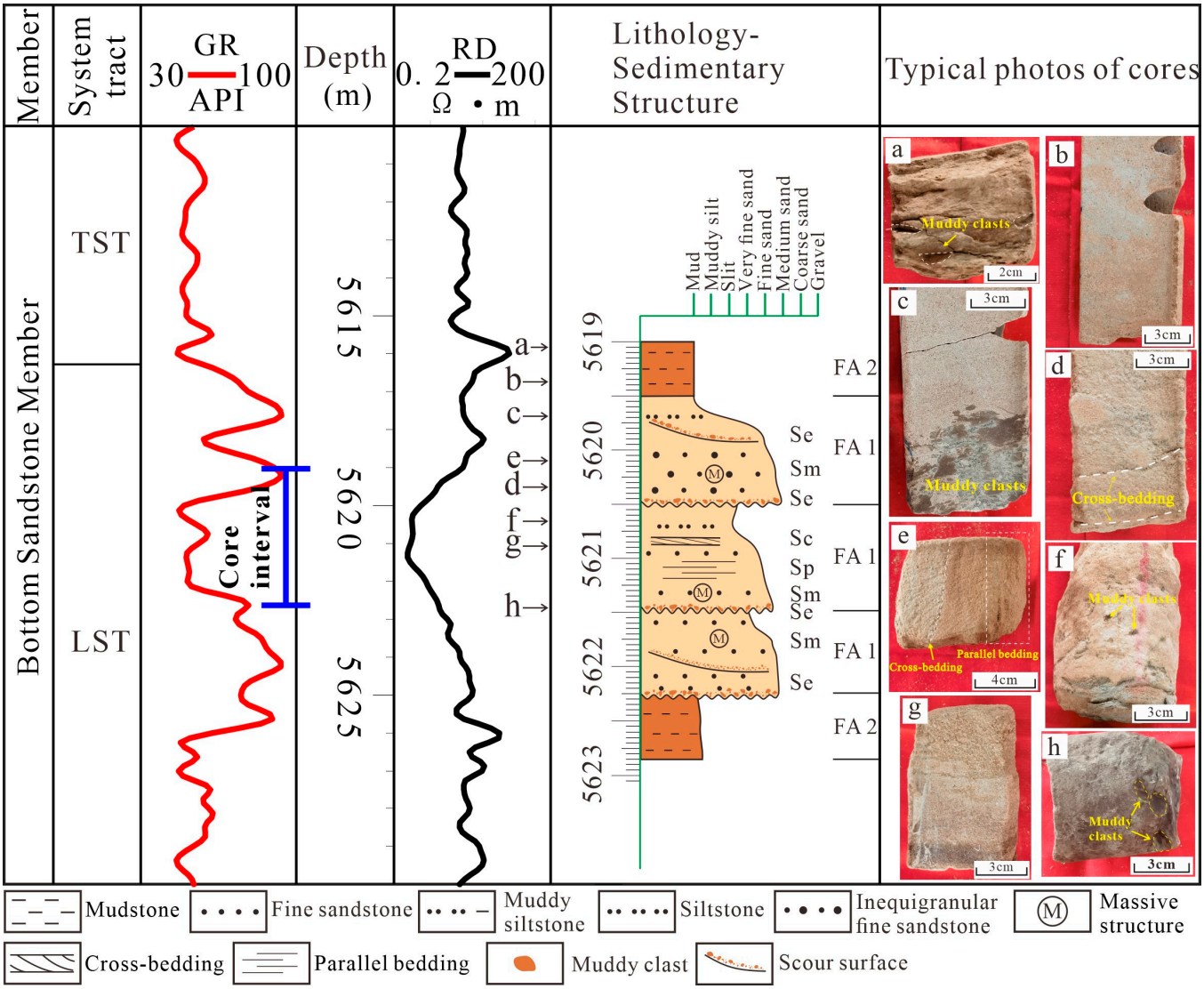


Figure 3. Lithology and sedimentary structure characteristics of the distributary channel in well PL103: (**a**) 5619.8 m, brownish-red fine sandstone with mud clasts; (**b**) 5620.15 m, brownish-red poorly sorted sandstone, massive structure; (**c**) 5620.48 m, brownish-red poorly sorted sandstone, mud clasts scour surface; (**d**) 5620.9 m, brownish-red fine sandstone, cross-bedding; (**e**) 5621.15 m, brownish-red fine sandstone, cross-bedding, parallel bedding; (**f**) 5621.45 m, brownish-red fine sandstone, mud clast scour surface; (**g**) 5621.68 m, brownish-red fine sandstone, massive structure; (**h**) 5622.3 m, brownish-red fine sandstone, mud clasts scour surface.

Interpretation: FA1 is interpreted as distributary channel deposits [59]. The normally graded, fining-upward sand bodies characteristic of distributary channels are controlled by a gradual decrease in flow velocity [60]. Brownish-red mud clasts and red sandstones were formed in an oxidizing environment [61]. Mud clasts (Se) provide evidence of channel scouring associated with flood events [59].

Interdistributary Bay (FA2)

Description: FA2 is mainly composed of reddish-brown mudstone and silty mudstone (Figure 4), with common dry cracking (Figure 4a) and a massive structure (Figure 4c), and contains layered gypsum (Figure 4b,d). The lithofacies of FA2 are primarily composed of Mmc, Mm, and Gm.

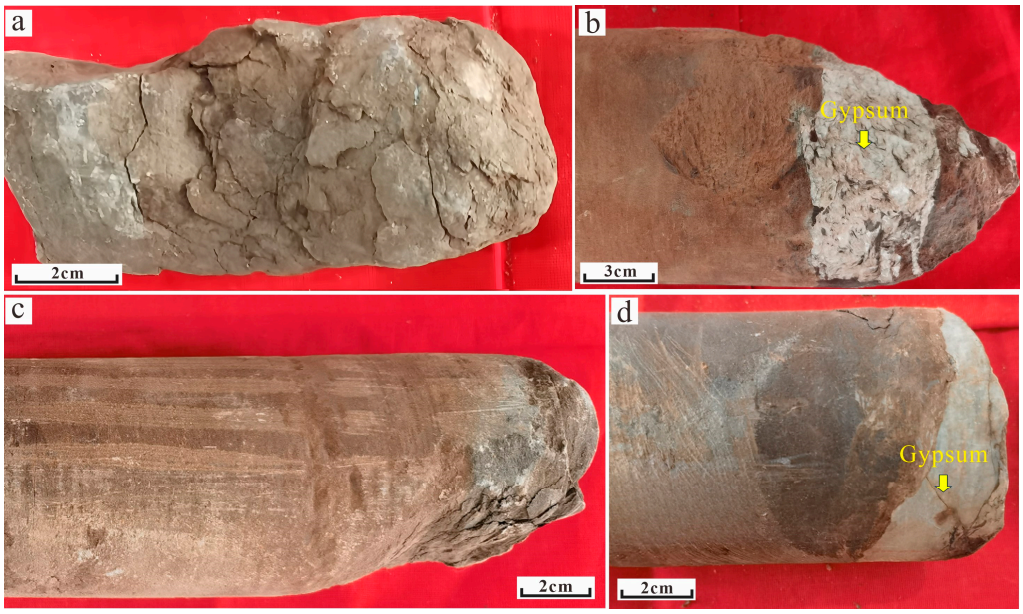


Figure 4. Core characteristics of the interdistributary bay. (**a**) Well PL6, 5882.6 m, brown mudstone with dry cracking features; (**b**) well PL101, 5668.1 m, brownish-red mudstone with thinly layered gypsum; (**c**) well PL102, brown silty mudstone with dry cracking features at the bottom; (**d**) well PL103, brown mudstone with massive structure and gypsum at the bottom.

Interpretation: FA2 is interpreted as interdistributary bay deposits [62]. The massive mudstone (Mm) is formed in low-energy, low-lying areas between distributary channels [63]. The dry cracking (Mmc) reflects the shrinkage and fracturing of mudstone after exposure and water evaporation [64]. Gypsum (Gm) forms through the evaporation, concentration, and crystallization of saline water, indicating a locally developed saline lake environment within the interdistributary bay [8].

4.1.2. Delta Front

Subaqueous Distributary Channel (FA3)

Description: FA3 is primarily composed of brown and light gray fine sandstone, with multiple normally graded sand bodies observed vertically (Figure 5). The base of single sand bodies often features scouring surfaces with gypsum clasts and mud clasts (Figure 6c,f) overlain by parallel bedding (Figure 6e) and cross-bedding (Figure 6d,e). Within the sandstone, poorly sorted, coarser-grained abrupt layers are present, with grain size gradually decreasing upward (Figure 6d). The top of FA3 commonly exhibits mudstone bands, bioturbation structures (Figure 6a,b), and ripple cross-bedding (Figure 6f). The lithofacies of FA3 are primarily composed of Se, Sp, Sc, Sr, Sh, and Smb.

Interpretation: FA3 is interpreted as subaqueous distributary channel deposits [25]. Compared with FA1, FA3 contains a higher proportion of fine-grained clastic material, reflecting a lower-energy environment. Gypsum clasts and muddy clasts (Se) are products of channel scouring and transport [7,65]. Coarser-grained abrupt layers within the sandstone represent hyperconcentrated flow deposits, serving as indicators of flood events [66]. Parallel bedding (Sp) and cross-bedding (Sc) indicate high sedimentation rates [67]. The mud drapes (Smb) at the top of FA3 reflect a significant decrease in hydrodynamic energy, leading to the deposition of fine-grained mud [68]; meanwhile, variations in flow velocity and direction contribute to the formation of ripple cross-bedding [69]. Bioturbation structures (Smb) are formed due to reduced hydrodynamic energy and increased nutrient availability, which enhance biological activity [70,71].

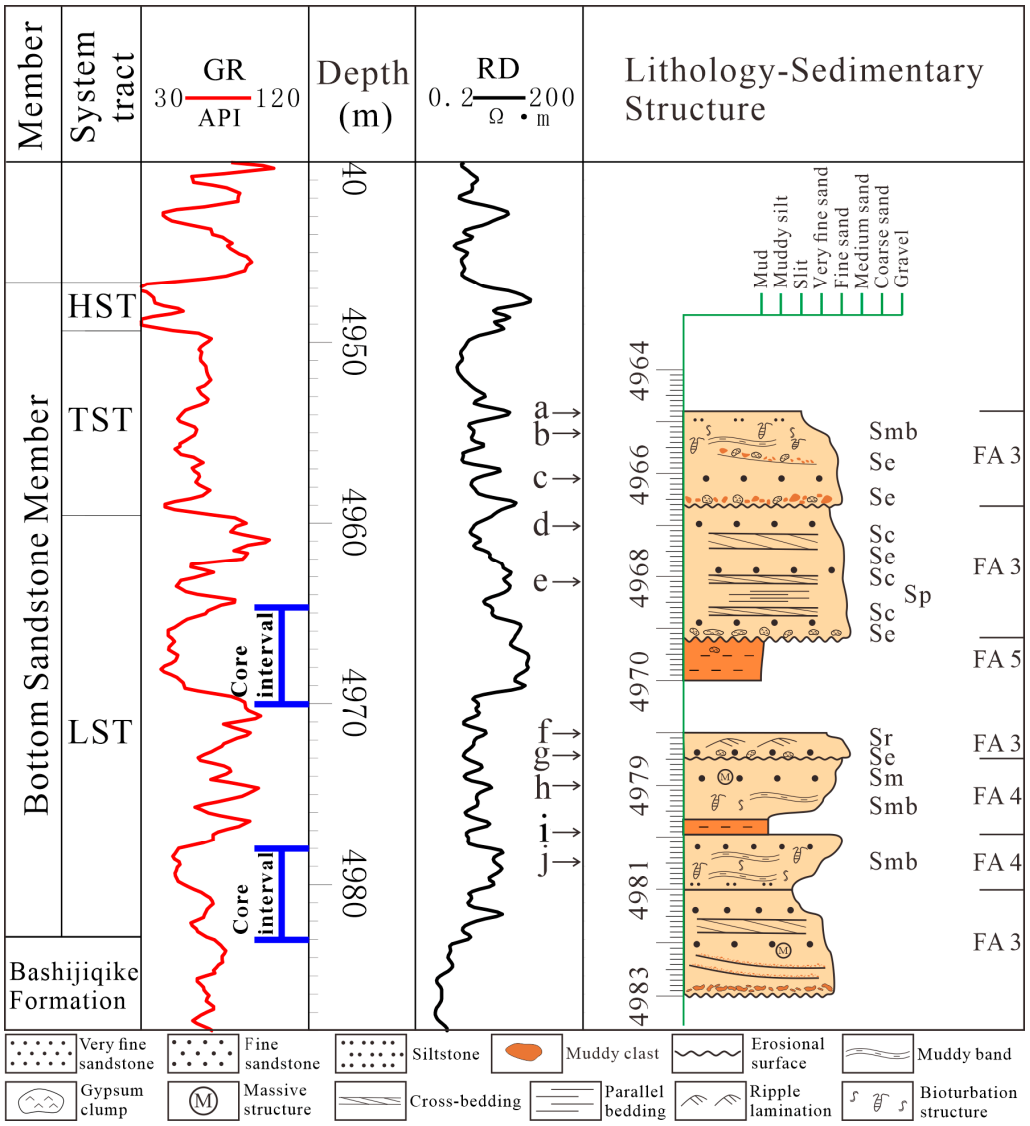


Figure 5. Well log characteristics and core section sketch of the subaqueous distributary channel and mouth bar from well WD101.

Mouth Bars (FA4)

Description: FA4 is primarily composed of brown very fine sandstone to fine sandstone, exhibiting a coarsening upward grain size trend (Figure 5). The bottom of FA4 is commonly characterized by muddy bands and bioturbation structures (Figure 6h,j), with a gradual decrease in mud content upward (Figure 6g,i). The top of FA4 is mainly composed of massive structures (Figure 6g). The sand body of FA4 is relatively thin, often less than 2 m, and is less developed in the study area. The main lithofacies of FA4 are Smb and Sm.

Interpretation: FA4 can be interpreted as mouth bar deposits [72]. Flow decelerates during the river's entry into the lake, causing sediment to accumulate at the river's mouth, forming a mouth bar [73]. Fine-grained sediments are initially deposited during the formation of mouth bars, and muddy bands (Smb) are formed under the influence of wave and tidal actions [74]. Frequent bioturbation in the mouth bar environment disrupts primary sedimentary structures and modifies the distribution of muddy bands [75]. The upward occurrence of massive structures (Sm) results from sand body progradation and enhanced hydrodynamics [59].

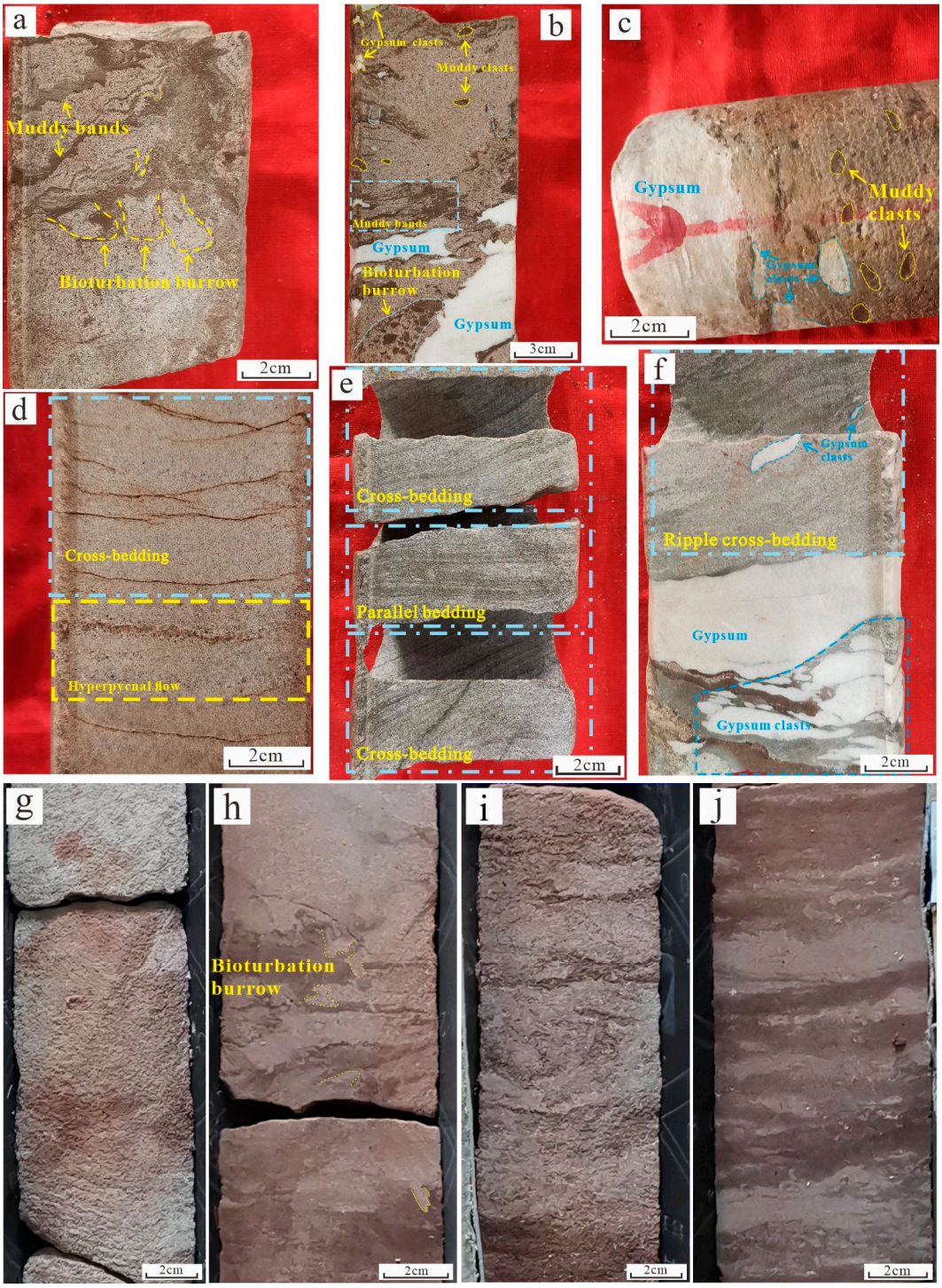


Figure 6. Core characteristics of subaqueous distributary channel (**a**–**f**) and mouth bar (**g**–**j**) from well WD101; core locations shown in Figure 5; (**a**) 5965.2 m, brown very fine-grained sandstone, developed bioturbation structures and muddy bands; (**b**) 4965.65 m, brown fine sandstone containing milky white gypsum lumps and gypsum clasts, with mud clasts, bioturbation structures, and muddy bands; (**c**) 4966.5 m, brown fine sandstone containing milky white gypsum lumps and gypsum clasts, mud clasts; (**d**) 4967.4 m, brown fine sandstone, hyperpycnal flow, cross-bedding; (**e**) 4968.5 m, gray fine sandstone, parallel bedding, cross-bedding; (**f**) 4978.4 m, gray fine sandstone, containing milky white gypsum lumps and gypsum clasts, with ripple cross-bedding; (**g**) 4978.85 m, light brown to light gray fine sandstone, massive structure; (**h**) 4979.4 m, brown very fine sandstone, muddy bands, bioturbation structures; (**i**) 4980.3 m, brown fine sandstone, muddy bands, bioturbation structures; (**j**) 4980.9 m, brown siltstone, muddy bands, bioturbation structures.

Subaqueous Interdistributary Bay (FA5)

Description: FA5 is primarily composed of brown and light green mudstone, silty mudstone, muddy siltstone, and gypsiferous mudstone (Figure 7), with gypsum commonly found within the strata (Figure 7b–g). FA5 develops sandy bands (Figure 7a), asymmetric wave bedding (Figure 7a), horizontal bedding (Figure 7g), gray-green muddy clasts (Figure 7e), gypsum clasts (Figure 7f,g), and bioturbation structures (Figure 7f,g). The main lithofacies of FA5 are composed of Mw, Mh, Mgc, and Msb.

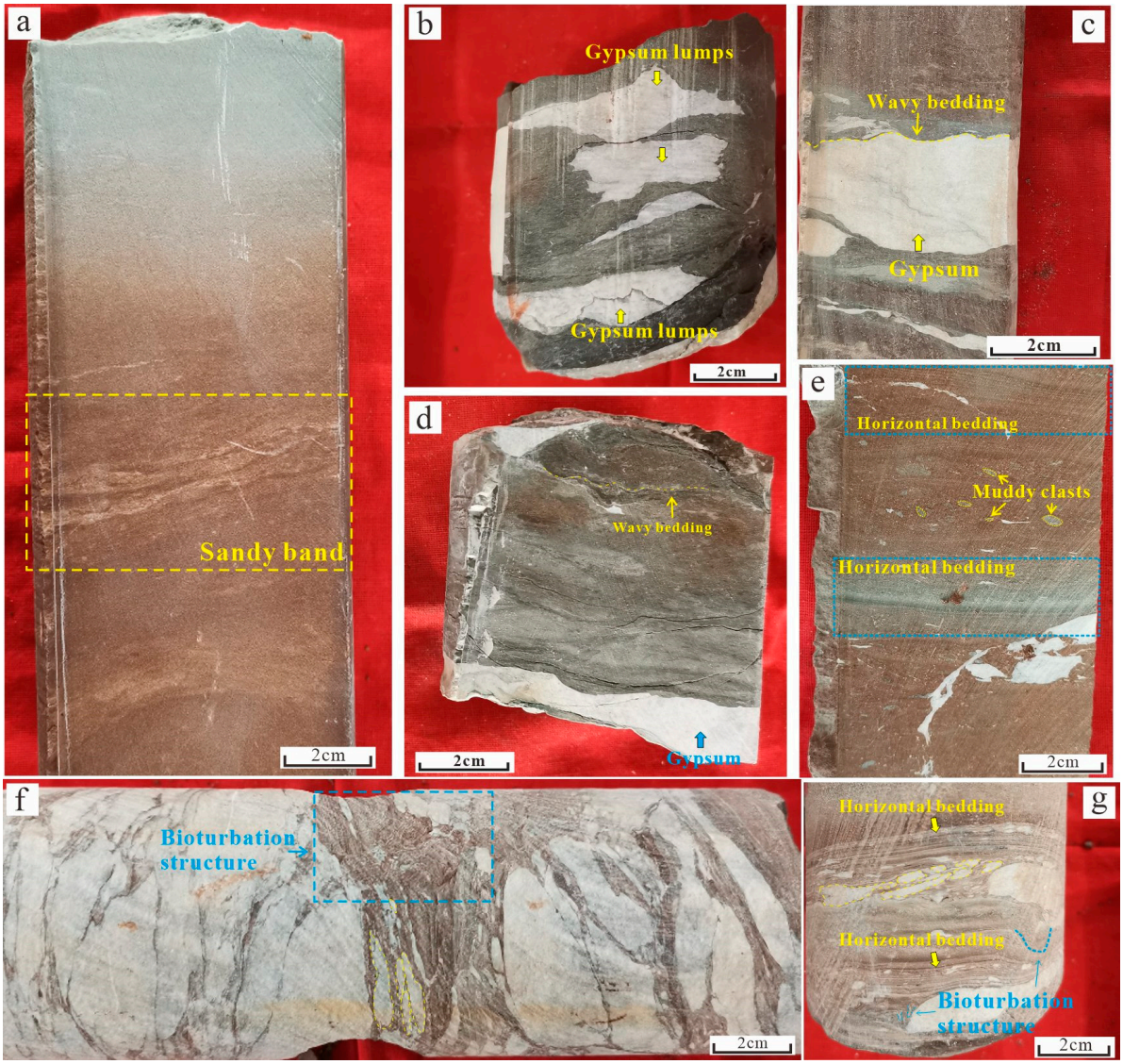


Figure 7. Core characteristics of subaqueous interdistributary bay. (**a**) Well WT502, 5398.7 m, brown-gray-green muddy siltstone, sandy bands; (**b**) well PL2, 5784.4 m, gray-green mudstone, gypsum lumps; (**c**) well PL102, 5624.5 m, brown-gray-green mudstone, with layered gypsum, wave bedding observed on gypsum surfaces; (**d**) well WD1, 5015.6 m, brown-grayish green mudstone, layered gypsum, wavy bedding; (**e**) well WT1, 5287.1 m, brown-grayish green mudstone, with grayish green mud clasts, horizontal bedding; (**f**) well WT8, 5287.3 m, brown gypsiferous mudstone, gypsum clumps, bioturbation structures; (**g**) well WT8, 5287.6 m, brown gypsiferous mudstone, silty mudstone, horizontal bedding, gypsum clasts.

Interpretation: FA5 can be interpreted as deposits of a subaqueous interdistributary bay [49]. The alternating brown and gray-green rocks result from seasonal fluctuations in lake levels under arid conditions. When the lake level drops, mudstones deposited in

reducing conditions are exposed, oxidizing and turning brown as oxygen increases [76]. The sandy bands (Msb) are formed by the deposition of sandy sediments carried into FA5 by waves [49]. Asymmetrical ripple structures (Mw) result from unidirectional currents transporting and depositing sediments along the flow direction [74]. Horizontal bedding (Mh) forms under relatively calm hydrodynamic conditions, with fine-grained materials settling by grain size and density under gravity [46]. The development of muddy clasts (Mgc) and gypsum clasts (Mgc) indicates flood events [7,77]. In arid climates, frequent fluctuations in hydrodynamic conditions promote the mixed deposition of evaporites and clastic rocks. Due to the relatively low hydrodynamic conditions, bioturbation structures (Mh) are commonly observed within subaqueous interdistributary bays [59].

4.1.3. Saline Lake

Sand Bar (FA6)

Description: FA6 is mainly composed of brown fine-grained sandstone, with relatively minor vertical grain size variation, exhibiting an overall upward coarsening grain size pattern. A large number of gypsum spots develop at the top (Figure 8b,c), and small-scale wave ripple cross-bedding is observed within the sandstone (Figure 8c,d). FA6 is relatively thin in the study area, typically less than 2 m thick (Figure 8), with overlying strata mainly consisting of gypsum layers (Figure 8a). The lithofacies of FA6 are mainly composed of Sgs and Sw. The grain size cumulative probability curve shows characteristics of two saltation components and one suspended component (Figure 8e), with the saltation components consisting of two straight segments with different slopes.

Interpretation: FA6 is interpreted as a sand bar deposit. Sand bars are formed by wave action, which erodes and transports clastic materials from the lake shore, depositing them near ancient uplifts or underwater highlands [78]. The wave ripple cross-bedding (Sw) is formed by the periodic changes in wave-induced currents, which transport and deposit sand grains, resulting in ripples oriented perpendicular to the wave propagation direction [56]. The gypsum spots (Sgs) are the result of evaporative crystallization of saline water in pores [43]. The grain size cumulative probability curve indicates a relatively complex hydrodynamic depositional environment, commonly observed in sand bars [79,80]. The coarser saltation components represent rapid scouring and transport by waves or alongshore currents, while the finer saltation components indicate periods of wave or current inactivity, when hydrodynamic conditions were weaker. The suspended components suggest the presence of turbulence in the water, keeping finer clastic materials in suspension and allowing for gradual deposition.

Shallow Littoral Lake (FA7)

Description: FA7 is mainly composed of gypsum (Figure 9a,d), gray-green mudstone (Figure 9a,c), gypsiferous mudstone (Figure 9b), and muddy gypsum (Figure 9e), forming interbedded layers of mudstone and gypsum. Horizontal bedding can be observed in the core (Figure 9c), with gypsum nodules distributed along the layers (Figure 9c). The lithofacies of FA7 are mainly composed of Gm, MG, Mh, and Mm.

Interpretation: FA7 is interpreted as a shallow littoral lake [5]. The interbedding of mudstone and gypsum indicates periodic fluctuations in seasonal climatic conditions and lake water salinity. The development of gypsiferous mudstone and muddy gypsum (MG) indicates that gypsum precipitation was influenced by terrigenous clastic input during evaporation [81]. The presence of red clastic impurities within the gypsum (Gm) (Figure 9e) indicates an oxidizing environment associated with subaerial exposure [76]. Gypsum nodules (Mm) are commonly found in sabkha environments and form during the early diagenetic stage [43].

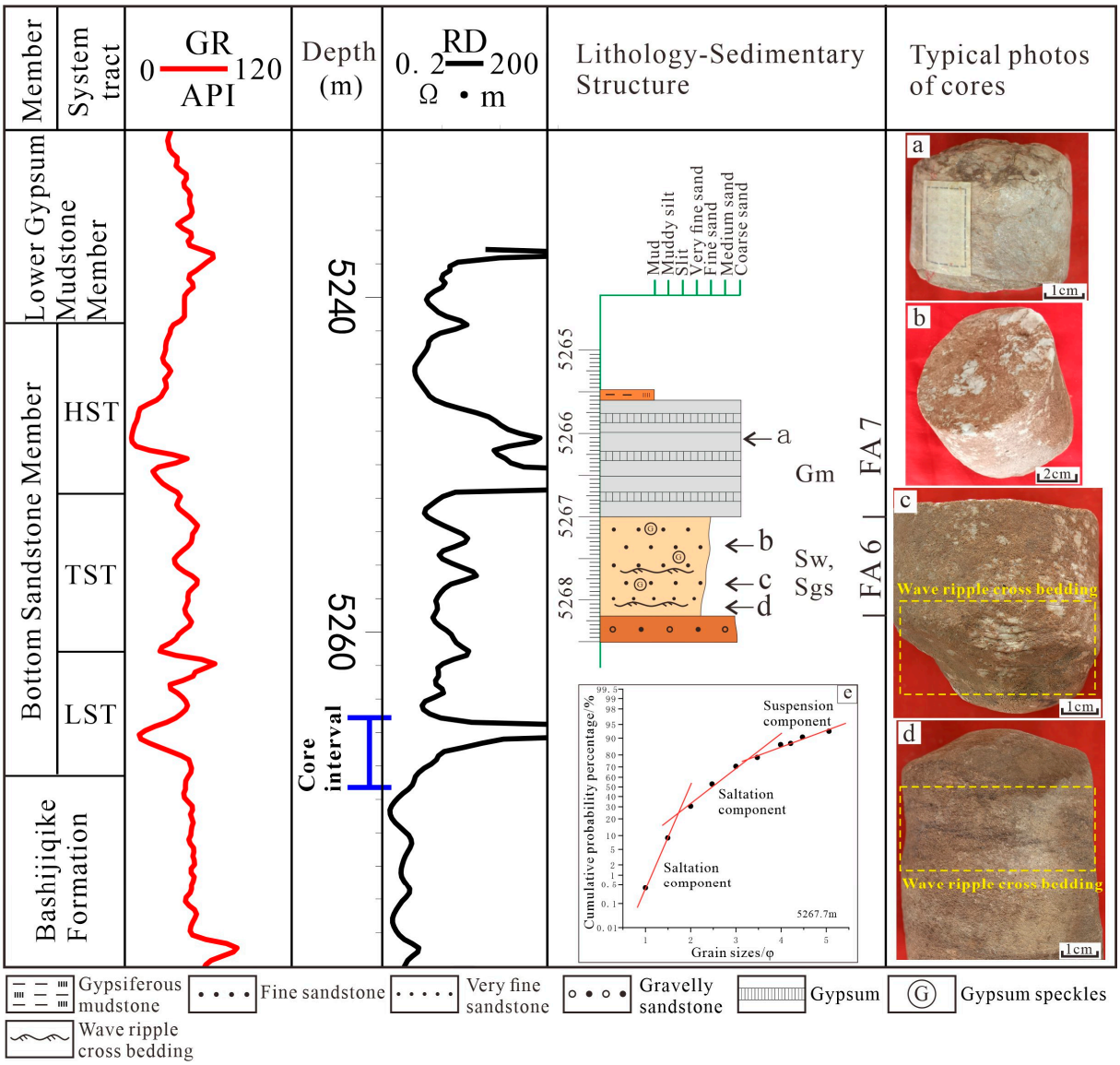


Figure 8. Lithological and sedimentary structure characteristics of the sand bar in well WT4. (**a**) 5266.05 m, pale yellow gypsum; (**b**) 5267.35 m, brown fine sandstone, spotted gypsum; (**c**) 5267.8 m, brown fine sandstone, spotted gypsum, wave ripple cross-bedding; (**d**) 5268.1 m, brown fine sandstone, wave ripple cross-bedding; (**e**) 5267.7 m, grain size cumulative probability curve.

4.2. The Occurrence Characteristics of Gypsum

4.2.1. Layered Gypsum

Layered gypsum mainly occurs in milky white (Figure 10a,e,g), grayish-white (Figure 10b,h), and light red (Figure 10c,d,f) colors, with a layered distribution. It forms abrupt contacts with the adjacent layers, which are predominantly mudstones (Figure 10). The layered gypsum exhibits features of massive, network, and dry-cracked structures. The massive gypsum is compositionally uniform and lithologically dense, with occasional asymmetric wavy bedding observed on its surface (Figure 10a,e,g). The network gypsum is characterized by multiple gypsum lumps separated by mud-filled (Figure 10c,d) or dolomitic-filled (Figure 10b,h) fractures. The gypsum lumps range from 2 to 5 cm in size and can grow vertically (Figure 10c,d,h) or in a flattened development (Figure 10b,d). The dry-cracked gypsum (Figure 10f) is characterized by irregular, wide fractures within the gypsum layers, which intersect and are filled with muddy material.

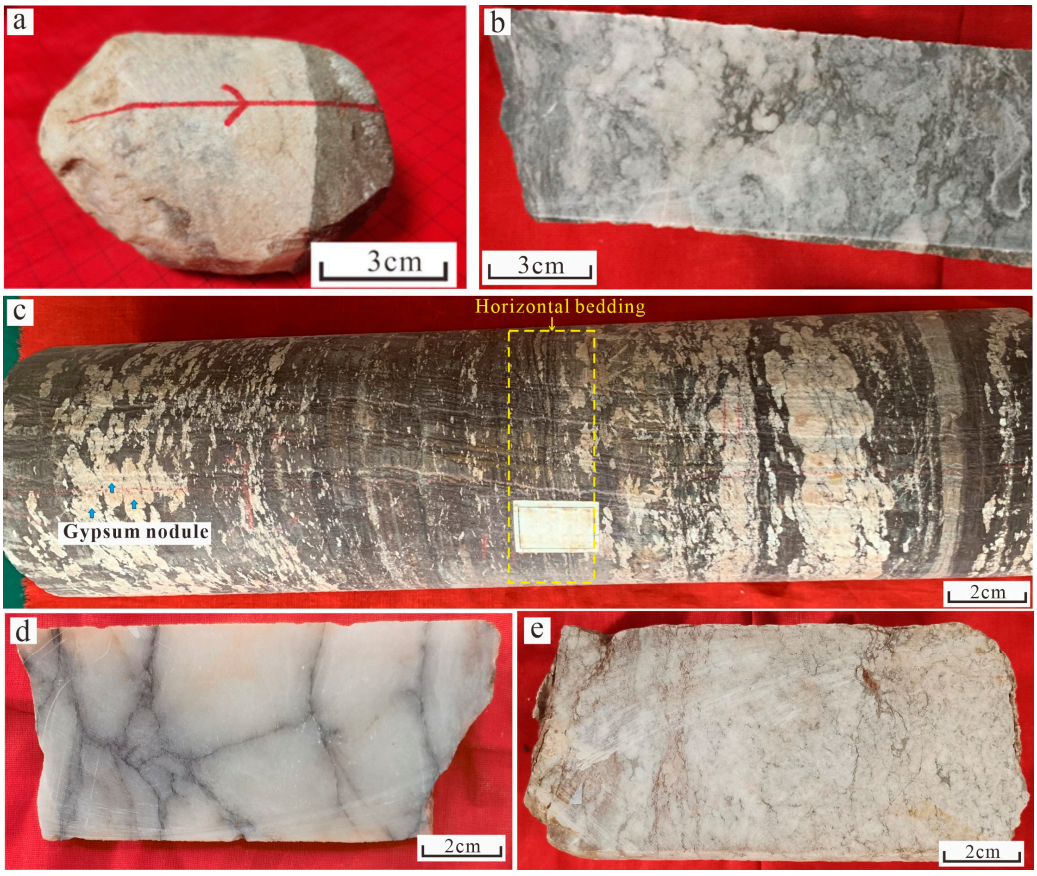


Figure 9. Core characteristics of the shallow littoral lake deposits. (**a**) WM61, 4826 m, layered gypsum, with gray-green mudstone developed at the base, sharp contact; (**b**) WM16, 4680.6 m, gypsiferous mudstone, with an indistinct boundary between gypsum and mudstone; (**c**) YH9, 5452.03 m, gray-green mudstone, with gypsum nodules developed along the layers, horizontal laminations; (**d**) WT5, 5293.5 m, network gypsum with fractures filled by dolomitic material; (**e**) WT3, 5330.4 m, light red layered gypsum.

4.2.2. Gypsum Clasts

The gypsum clasts are predominantly milky white, embedded within clastic rocks, and display sharp contacts with the surrounding matrix. Based on their morphology, they can be classified into four types: tear-shaped (Figure 11d), cloud-like (Figure 11i,j), conglomeratic-textured (Figure 11g), and flat-elliptical (Figure 11a–c,e,f,h). The tear-shaped gypsum clasts (Figure 11d) exhibit angular forms, with variable shapes and sizes, and individual clasts can reach up to the decimeter scale. The cloud-like gypsum clasts (Figure 11i,j) exhibit a cloud shape or irregular form with sub-angular to sub-rounded edges. Most gypsum clasts are over 5 cm in size. The surrounding rocks mainly consist of very fine sandstone to fine sandstone. Conglomeratic-textured gypsum clasts (Figure 11g) exhibit sub-angular to sub-rounded forms, with clast sizes mostly greater than 3 cm. Multiple clasts often cluster together, and the surrounding rocks are mainly fine-grained sandstone. The flat-elliptical gypsum clasts have their long axes approximately parallel to the bedding planes, and they are commonly arranged in dense clusters (Figure 11b,c,e,f); however, they may also occur as isolated clasts (Figure 11a,h). The surrounding rocks are mainly very fine sandstone to mudstone with muddy clasts. The flat-elliptical gypsum clasts are generally sub-rounded to rounded and mostly smaller than 3 cm in size.

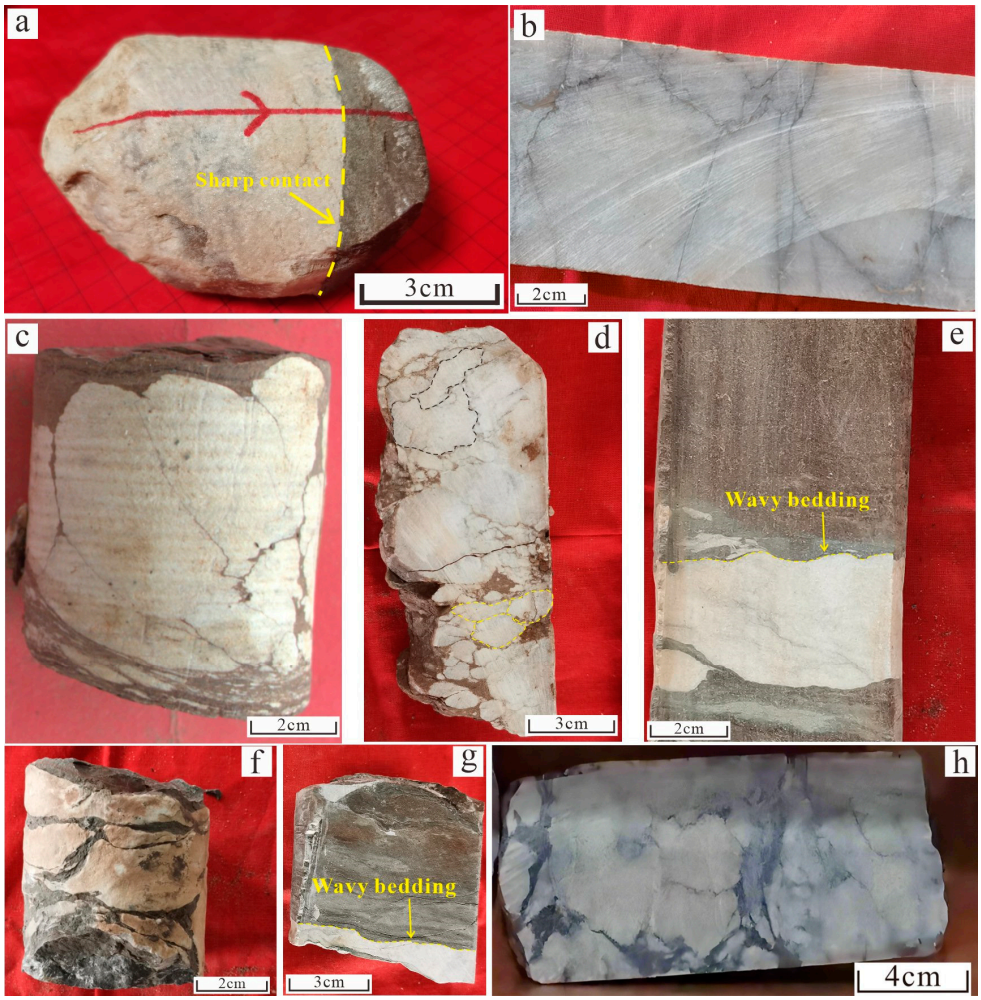


Figure 10. Core characteristics of layered gypsum. (**a**) WM61, 4826 m, milky white layered gypsum; (**b**) WT5, 5293.5 m, grayish-white network gypsum with fractures filled by dolomitic material; (**c**) WM16, 4665.7 m, reddish-brown mudstone with light red network gypsum; gypsum lumps exhibit vertical structures, and fractures are filled with muddy material; (**d**) WT3, 5330.4 m, pale red network gypsum, with the upper part exhibiting vertical structures and the lower part showing flattened and elliptical structures; (**e**) PL102, 5624.5 m, milky white layered gypsum exhibits asymmetric wavy bedding on its surface, with grayish-green mudstone as the surrounding rock and brown mudstone above; (**f**) WD5, 5142.4 m, grayish-white dry-cracked gypsum, with muddy material filling the gaps between the gypsum; (**g**) WD1, 5015.6 m, milky white layered gypsum exhibits asymmetric wavy bedding on its surface, with grayish-green mudstone as the surrounding rock; (**h**) WT5, 5294.1 m, grayish-white network gypsum, with dolomitic material filling the gaps between the gypsum, which exhibits a vertical structure.

4.2.3. Spotted Gypsum

Spotted gypsum within the clastic rocks occurs both as larger spots (Figure 12a,d) and as densely distributed smaller spots (Figure 12b–d). Larger spotted gypsum (Figure 12a,c,d) is irregular in shape, with poorly defined boundaries against the surrounding rock. This type of gypsum is smaller than 1 cm, occurring in a dispersed manner. Microscopically, the gypsum often aggregates as crystals with well-defined geometrical shapes, such as tabular and columnar forms (Figure 12h).

The finer spotted gypsum ranges in diameter from millimeters to micrometers and appears as small white particles adhering to the core surface (Figure 12b–d). These gypsum spots are scattered throughout the matrix without obvious clustering. When abundant, the

core surface may exhibit a hazy appearance (Figure 12b,d). Microscopically, gypsum occurs in pores either as cement (Figure 12e–g) or crystals (Figure 12e,i).

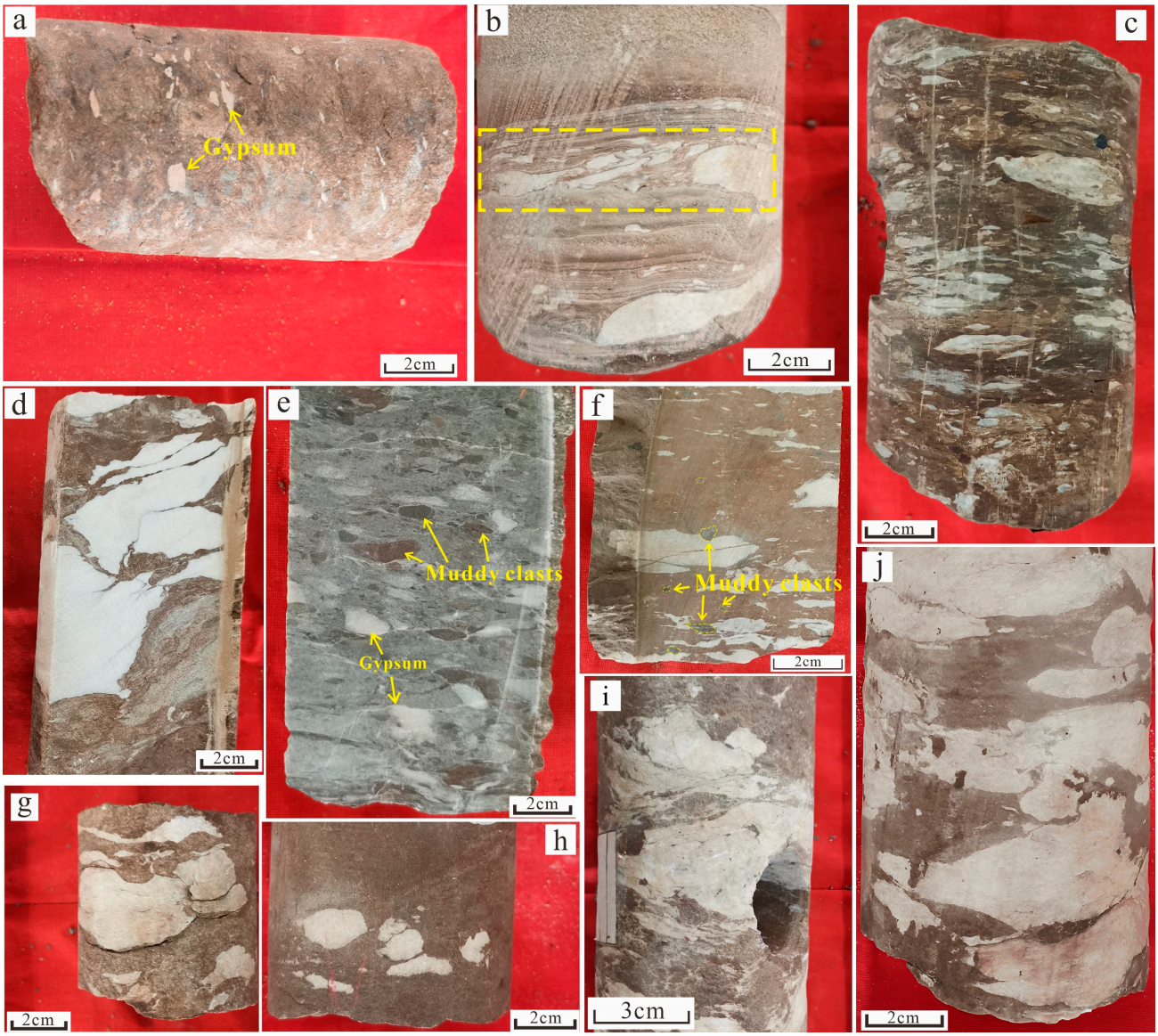


Figure 11. Core photographs of gypsum clasts. (**a**) PL101, 5627.7 m, brown very fine sandstone, flat-elliptical gypsum clasts, isolated distribution; (**b**) WT8, 5287.6 m, brown muddy siltstone, flat-elliptical gypsum clasts; (**c**) WT1, 5277.9 m, brown mudstone, flat-elliptical gypsum clasts; (**d**) WD102, 5231.3 m, brown siltstone, tear-shaped gypsum clasts; (**e**) WT1, 5277 m, gray-green gypsiferous mudstone, gray-green mud clasts, flat-elliptical gypsum clasts; (**f**) WT1, 5291.9 m, brown mudstone, gray-green mud clasts, flat-elliptical gypsum clasts; (**g**) WT8, 5285 m, brown fine sandstone, conglomeratic-textured gypsum clasts; (**h**) PL101, 5672 m, brown muddy siltstone, flat-elliptical gypsum clasts; (**i**) WD8, 5284.6 m, brown fine sandstone, cloud-like gypsum clasts; (**j**) WT5, 5313.4 m, brown very fine sandstone, cloud-shaped gypsum clasts.

4.2.4. Gypsum Nodule

This type of gypsum mainly occurs as sub-rounded to elliptical nodules (Figure 13a–c,e,f), though angular forms also occur (Figure 13d). Nodule sizes vary considerably, with diameters ranging from a few millimeters to up to 10 cm. Their color is typically milky white (Figure 13b,d,f) or pale yellow (Figure 13a,c,e). The gypsum nodules have sharp boundaries with the surrounding rocks, which are mainly mudstone and muddy siltstone.

On the core profiles, two distribution patterns are observed: isolated (Figure 13b,d,e) and clustered (Figure 13a,c,f). Isolated nodules occur singly, while clustered ones are densely packed, often in contact or compressed against each other. In these clusters, large nodules are typically surrounded by smaller ones. Clustered nodules exhibit both random (Figure 13f) and oriented (Figure 13a,c) arrangements. Randomly distributed nodules appear scattered and lack a clear pattern (Figure 13f), whereas oriented nodules exhibit consistent long-axis alignment and vertical rhythmicity (Figure 13c). Microscopically, the gypsum nodules are composed predominantly of platy, acicular, and fibrous crystals (Figure 13g–i). The crystals are arranged in oriented subdomains.

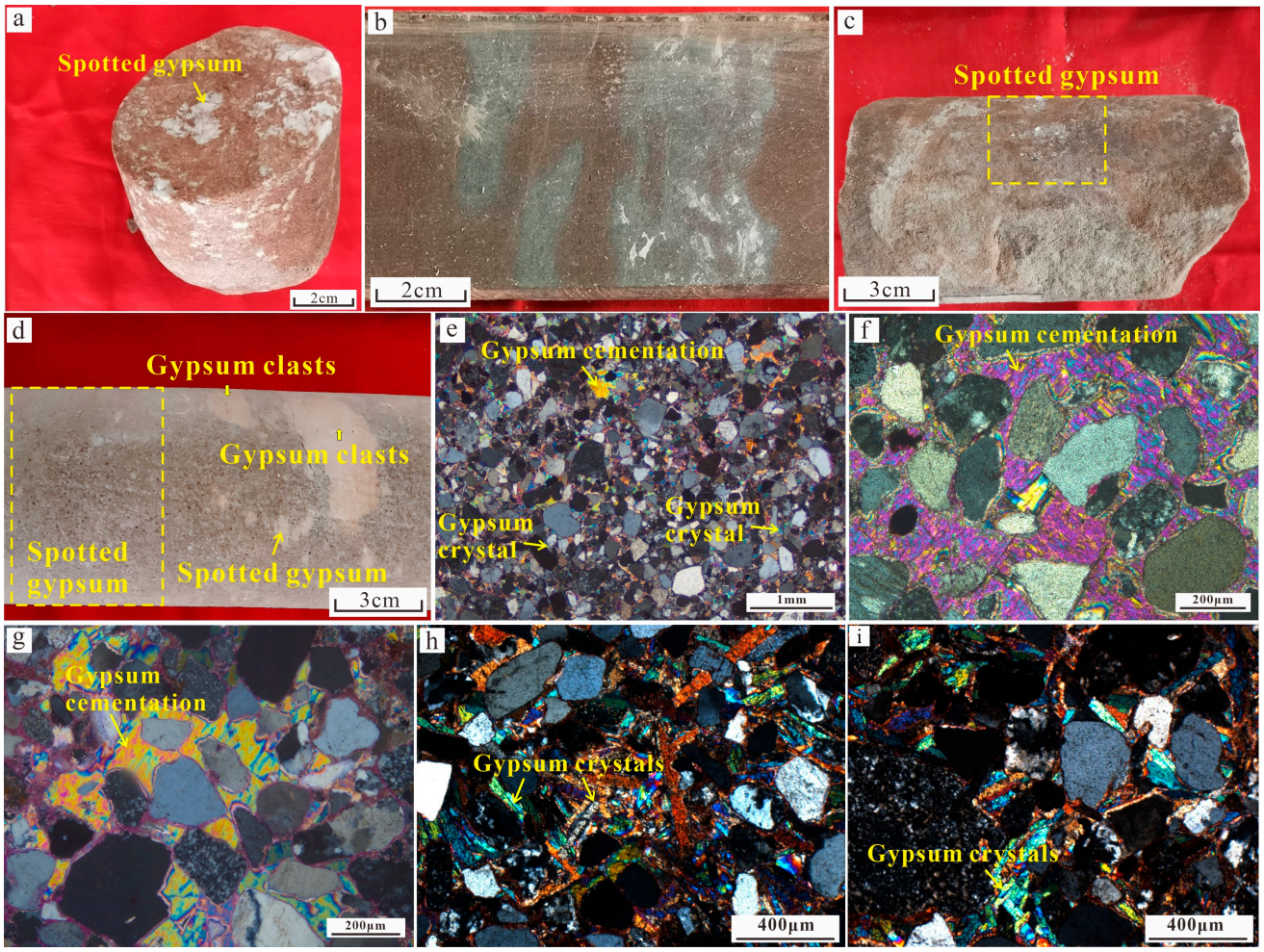


Figure 12. Core of spotted gypsum (**a**–**d**) and microfeatures (**e**–**i**). (**a**) WT4, 5267.35 m, brown fine sandstone, coarsely spotted gypsum; (**b**) WT5, 5307.4 m, brown-grayish green mudstone, spotted gypsum intercalated between clastic particles; (**c**) WT502, 5409.6 m, gray fine sandstone with spotted gypsum; (**d**) QM1, 5434.3 m, gray fine sandstone with spotted gypsum, gypsum clasts; (**e**) WT502, 5409.7 m, microfeatures of gypsum under cross-polarized light, showing colors, with gypsum filling the pores of the sandstone in the form of crystals and cement; (**f**) WD2, 4691.5 m, gypsum filling the pores in the form of cement; (**g**) WT502, 5404.2 m, gypsum filling the pores in the form of cement; (**h**) PL101, 5659.4 m, gypsum crystals filling the pores; (**i**) PL101, 5664.5 m, gypsum crystals filling the pores.

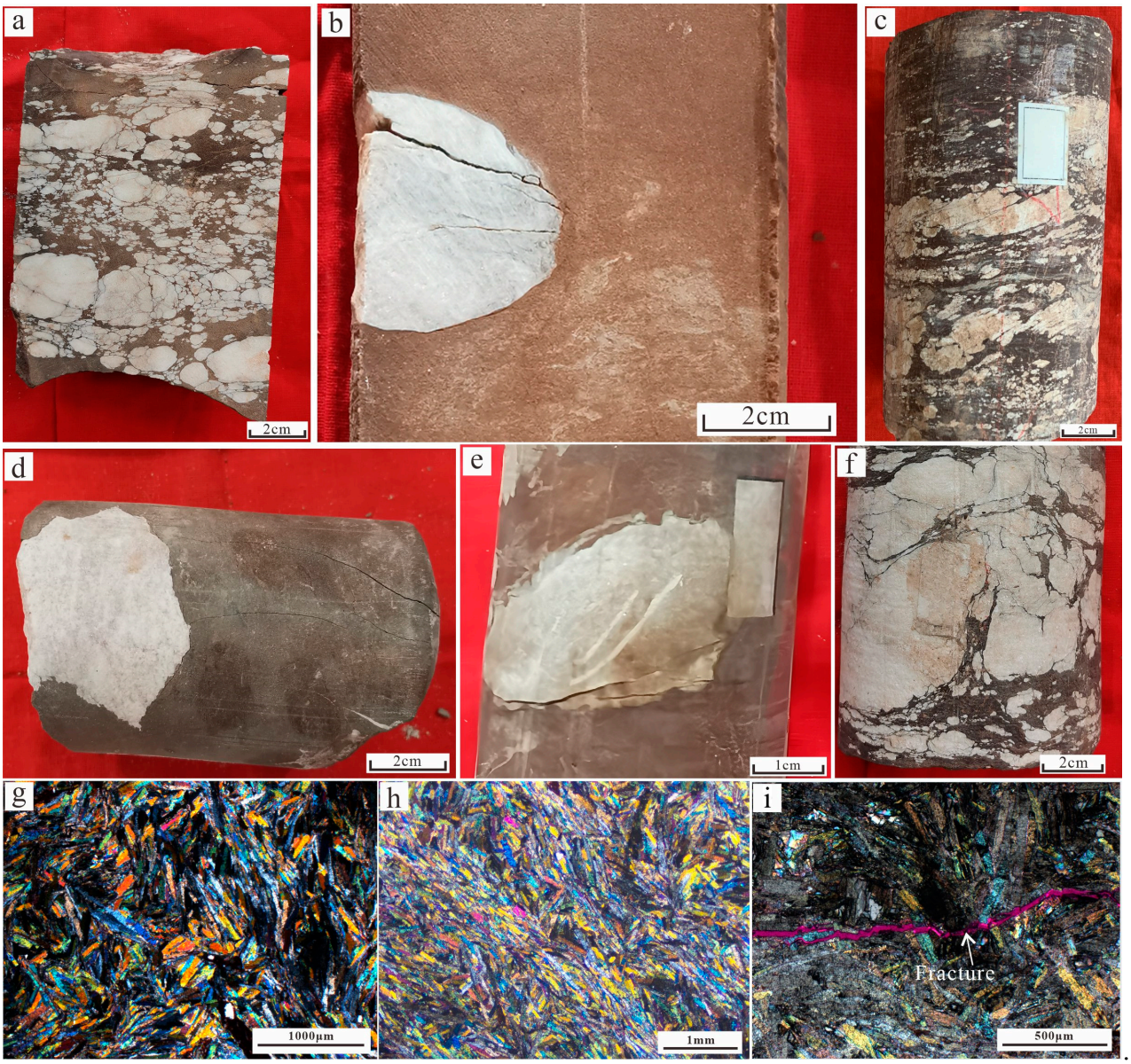


Figure 13. Core and microscopic characteristics of gypsum nodules. (**a**) YH3, 5132.6 m, brown mudstone with densely developed elliptical gypsum nodules, where large nodules are often surrounded by smaller ones; (**b**) WD101, 4969.5 m, brown muddy siltstone with elliptical gypsum nodules; (**c**) YH9, 5452.03 m, gypsum nodules distributed along bedding planes, overall inclined in one direction, with gray mudstone as the host rock. (**d**) PL2, 5785.1 m, angular gypsum nodules hosted by gray mudstone; (**e**) PL6, 5902.8 m, elliptical gypsum nodules hosted by brown mudstone; (**f**) YH3, 5134.7 m, densely developed gypsum nodules, with most nodules being elliptical; large nodules are typically surrounded by numerous smaller ones, hosted by brown mudstone. (**g**–**i**) Photomicrographs of gypsum nodules under cross-polarized light, showing multiple oriented subdomains with predominant development of acicular, platy, and fibrous gypsum crystals; (**g**) WD101, 4969.5 m; (**h**) YH3, 5134.7 m; (**i**) YH3, 5133.5 m.

4.2.5. Mixed Deposition of Clastic Rocks and Gypsum

Mixed lithologies of clastic material and gypsum include muddy gypsum (Figure 14a), gypsiferous mudstone (Figure 14c), gypsiferous mudstone containing muddy clasts (Figure 14b), and sandy gypsum (Figure 14d). In these rocks, the gypsum is impure, and its boundary with the clastic components is indistinct. In muddy gypsum, the gypsum content is relatively high, occurring in layered or cloud-like forms coexisting with muddy

clastic material, occasionally accompanied by small mud clasts (Figure 14a). In gypsiferous mudstone, the mud content is dominant, and gypsum typically appears in a misty or diffuse form within the mudstone matrix (Figure 14c). Gypsiferous mudstone with mud clasts contains poorly sorted muddy and gypsum clasts, most of which are under 2 cm in diameter (Figure 14b). Sandy gypsum has a rough surface, contains abundant sandy particles, and appears pale yellow (Figure 14d).

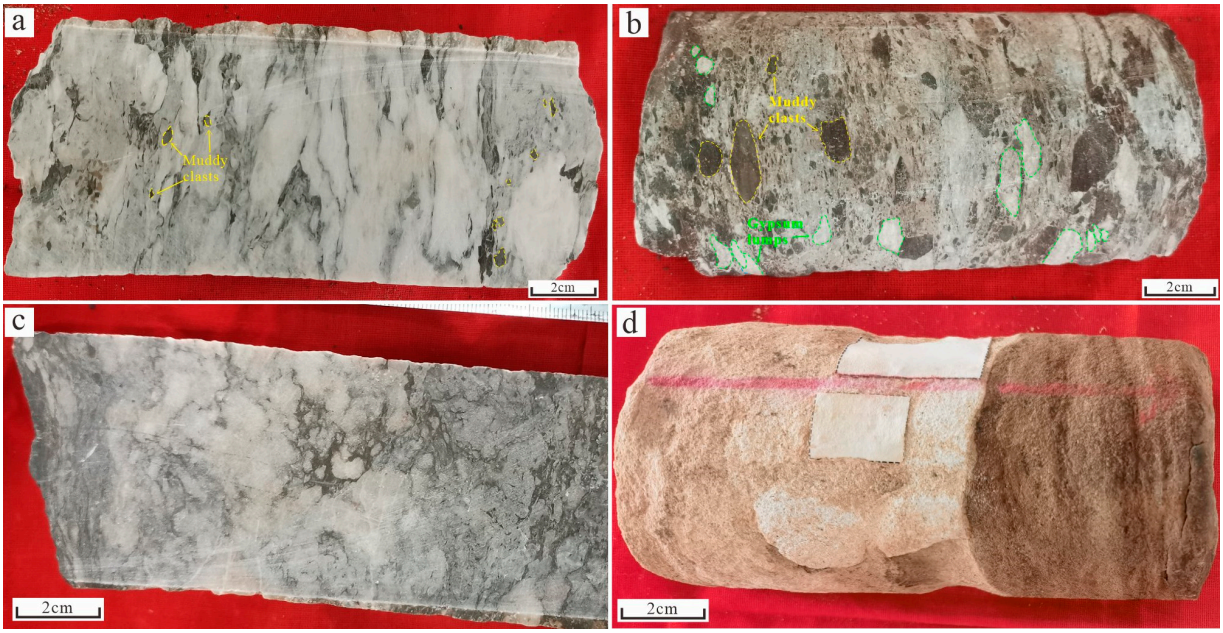


Figure 14. Core and microscopic characteristics of clastic rocks mixed with gypsum. (**a**) WT1, 5275.7 m, muddy gypsum with a milky white to light gray cloudy texture, containing muddy clasts; (**b**) WT1, 5276.9 m, gypsiferous mudstone containing muddy clasts; (**c**) WM16, 4680.6 m, gypsiferous mudstone; (**d**) PL103, 5616.1 m, light yellow sandy gypsum.

5. Discussion

5.1. Genesis of Gypsum with Different Occurrences

Previous studies analyzing the sulfur isotopes of gypsum have suggested that its composition is consistent with the $\delta^{34}S$ values of contemporaneous global seawater, reflecting a clear marine source signature [82]. During the deposition of the Paleogene Bottom Sandstone Member, influenced by intermittent marine transgressions from the Tethys Ocean, the lake basins in the northern Tarim Basin had limited connectivity with the sea [37,38]. Coupled with the arid climate at the time, a saline lake–delta depositional environment developed in the study area [83,84]. Under an arid climate, frequent seasonal variations in the region control the intensity of terrigenous material input, resulting in complex and variable hydrodynamic conditions [85,86]. These factors influence the crystallization and precipitation of gypsum in the lake basin, leading to the formation of gypsum with diverse morphologies.

5.1.1. Layered Gypsum

Layered gypsum is generally considered a subaqueous depositional product formed under stagnant water conditions with limited terrigenous input and within a relatively enclosed water body [87,88]. Previous studies have shown that dense massive gypsum typically forms as a primary chemical precipitate on flat surfaces below the wave base in shallow marine settings [87]. In saline lake–deltaic systems, dense, massive gypsum commonly develops in shallow lacustrine zones or in small lakes within subaqueous

interdistributary bays, particularly in areas where the water body has not completely dried up (Figure 15B,C). Massive gypsum exhibits an abrupt contact with the mudstone (Figure 15B(b),C(c)), indicating increased water salinity and reduced or ceased terrigenous input. Due to seasonal variations, this facies commonly presents a vertical succession of grayish-green mudstone–gypsum layer–grayish-green mudstone.

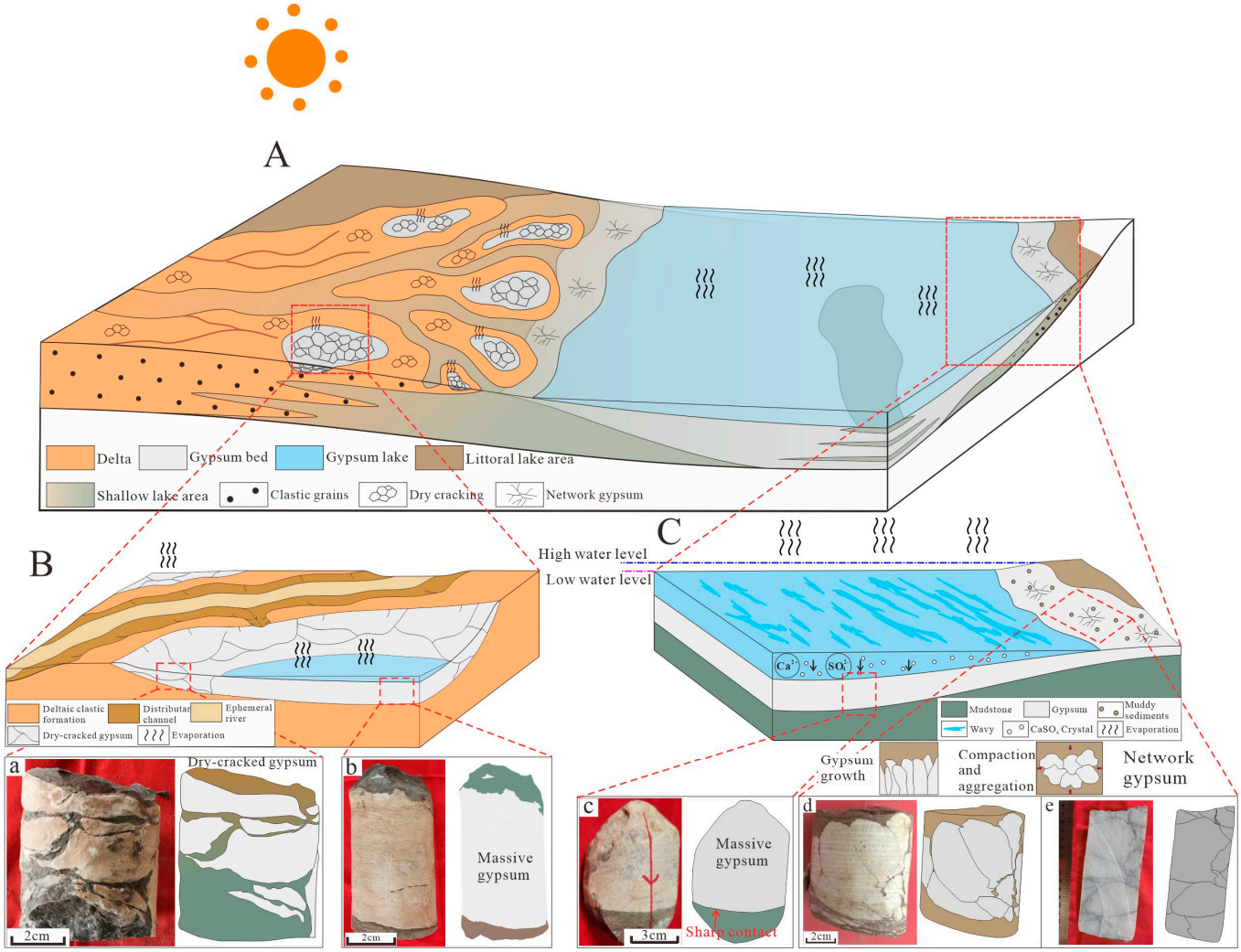


Figure 15. Layered gypsum deposition model. (**A**) Dry period saline lake–delta deposition model; (**B**) layered gypsum deposition model in the interdistributary bay of delta plain or its front; (**C**) depositional model of layered gypsum in shallow lacustrine areas; (**a**) WD5, 5142.4 m, dry-cracked gypsum; (**b**) PL102, 5745.5 m, dense massive gypsum; (**c**) WM61, 4826 m, dense massive gypsum, abruptly in contact with underlying mudstone; (**d**) WM901, 4665.7 m, network gypsum; (**e**) WT5, 5293.5 m, network gypsum.

As the saline lake continued to evaporate and dry up, the exposed gypsum underwent rapid dehydration, resulting in dry-cracked gypsum (Figure 15B(a)) [89]. The delta in the study area is characterized by red clastic rocks with high iron content, and during gypsum crystallization, iron ions may have been incorporated into the crystal structure, giving the gypsum a light-yellow color (Figure 15B(a,b)).

In continental saline lake environments, reticulate gypsum commonly develops in the marginal lacustrine zones (Figure 15C(d,e)), controlled by periodic fluctuations of the lake level. Intense evaporation facilitates the massive precipitation of primary gypsum crystals. As sedimentation continues, these crystals become buried within a matrix of mudstone

or dolomite and undergo early diagenetic aggregation, alignment, and fusion. The pore spaces provide a favorable environment for gypsum crystal growth and recrystallization. The muddy or dolomitic matrix is expelled with continued compaction, allowing gypsum crystals to come into contact and compact, eventually forming a network structure [4,90,91].

5.1.2. Gypsum Clasts

Elorza et al. (1998) [92] observed in the Ebro Basin that during rainfall events, surface runoff can erode gypsum-containing layers, transporting gypsum clasts from higher to lower areas. This transport process is associated with river discharge and flow velocity. Therefore, gypsum can undergo mechanical transport under the influence of rivers. Although gypsum is highly soluble in water, once its content exceeds the solubility limit, it will be transported and deposited in the form of clasts.

Core observations show that there are regular changes in gypsum's grain size, roundness, sorting, and morphology with increasing transport distance (Figure 16). Gypsum that formed early was damaged and eroded under the influence of river action (Figure 16B(e)), with the clastic materials being transported downstream together. As the transport distance increased, the gypsum's morphology evolved from tear-shaped, cloud-like, and conglomeratic-textured to flat-elliptical gypsum clasts (Figure 16B(f–i)). The grain size of gypsum clasts gradually decreased, roundness increased, and sorting improved. The grain size of the surrounding rock also gradually decreased during the transport process, reflecting a gradual reduction in hydrodynamic energy. Since the study area is relatively far from the source, the surrounding rock is generally finer than fine sandstone (Figure 16B(a–d)). Among them, flat-elliptical gypsum clasts have been transported over long distances, and the surrounding host rock is generally finer than very fine sandstone (Figure 16B(d)).

5.1.3. Spotted Gypsum

Spotted gypsum forms mainly during the early diagenetic stage. After the deposition of clastic rocks, the sand bodies are buried in a shallow manner. During the evaporation and concentration of overlying saline lake water or capillary water, gypsum crystals begin to precipitate and fill the intergranular pores between sandstone grains (Figure 17a). At this stage, the pore space has not yet undergone significant compaction, allowing the crystals to grow relatively freely between grains while preserving their complete crystal forms. Compared with gypsum crystals that grow freely within pores, gypsum cement (Figure 17b) formed during early diagenesis typically develops in a relatively closed fluid system with stronger compaction and more limited pore space.

Late-diagenetic gypsum cements are also present in the study area. Microscopically, they show scaly or microcrystalline mosaic textures, lack euhedral prismatic forms, and often cut across grain boundaries with an "invasive" appearance. These cements, which are controlled by deep fluid migration and ionic enrichment, are minimally affected by seasonal hydrochemical variations and are therefore not discussed in detail here.

5.1.4. Gypsum Nodule

In the study area, gypsum nodules are commonly observed in subaqueous interdistributary bays of the delta front and in the littoral, shallow lacustrine zones. Previous studies have suggested that the development of these nodules is closely linked to early diagenesis and is controlled by the pore structure of detrital sediments [93,94].

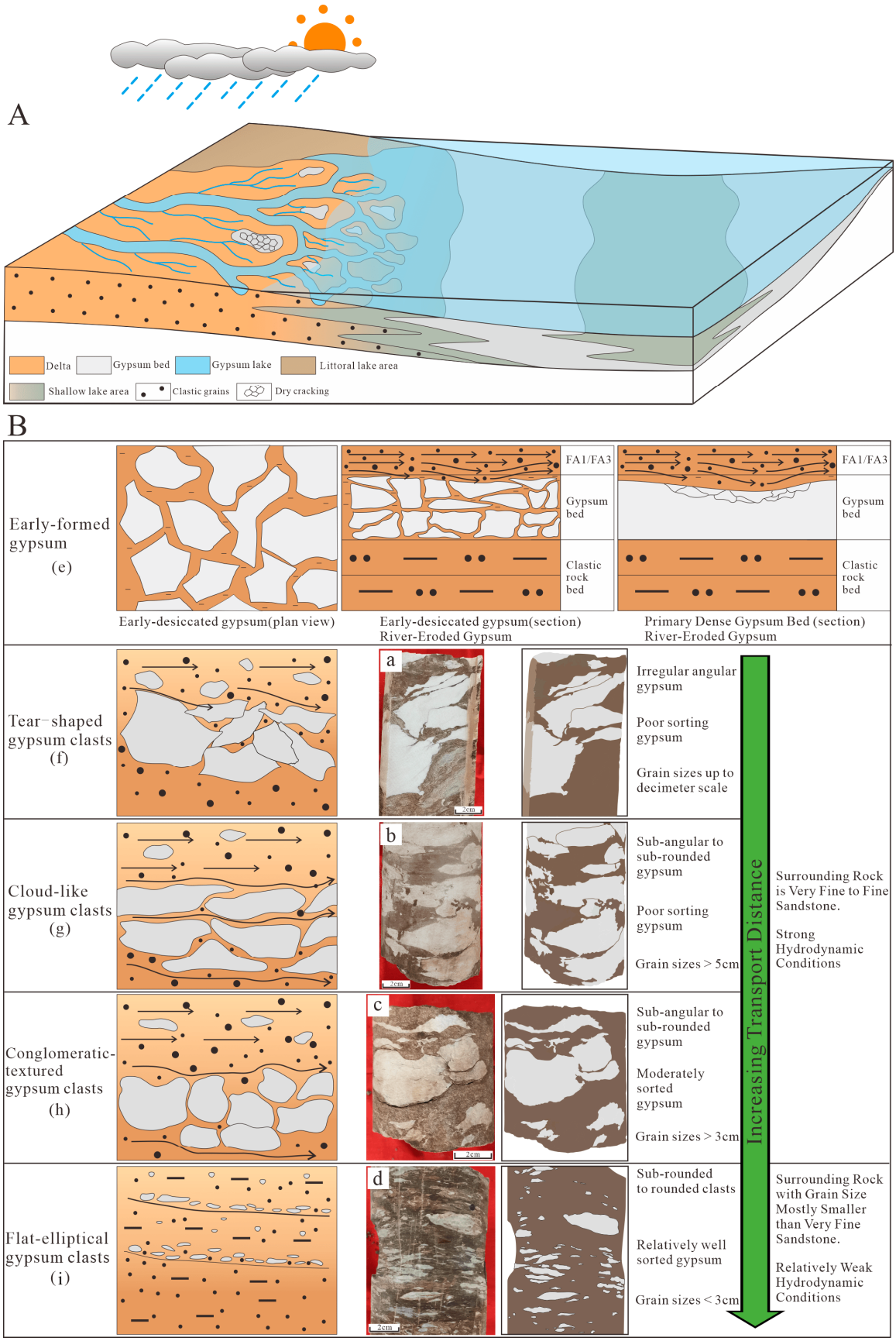


Figure 16. Gypsum clasts deposition model. (**A**) Flood period salt lake–delta deposition model; (**B**) destruction and transport of gypsum by river. (**a**) Well WD102, 5231.3 m; (**b**) well WT5, 5313.4 m; (**c**) well WT8, 5285 m; (**d**) well WT1, 5277.9 m.

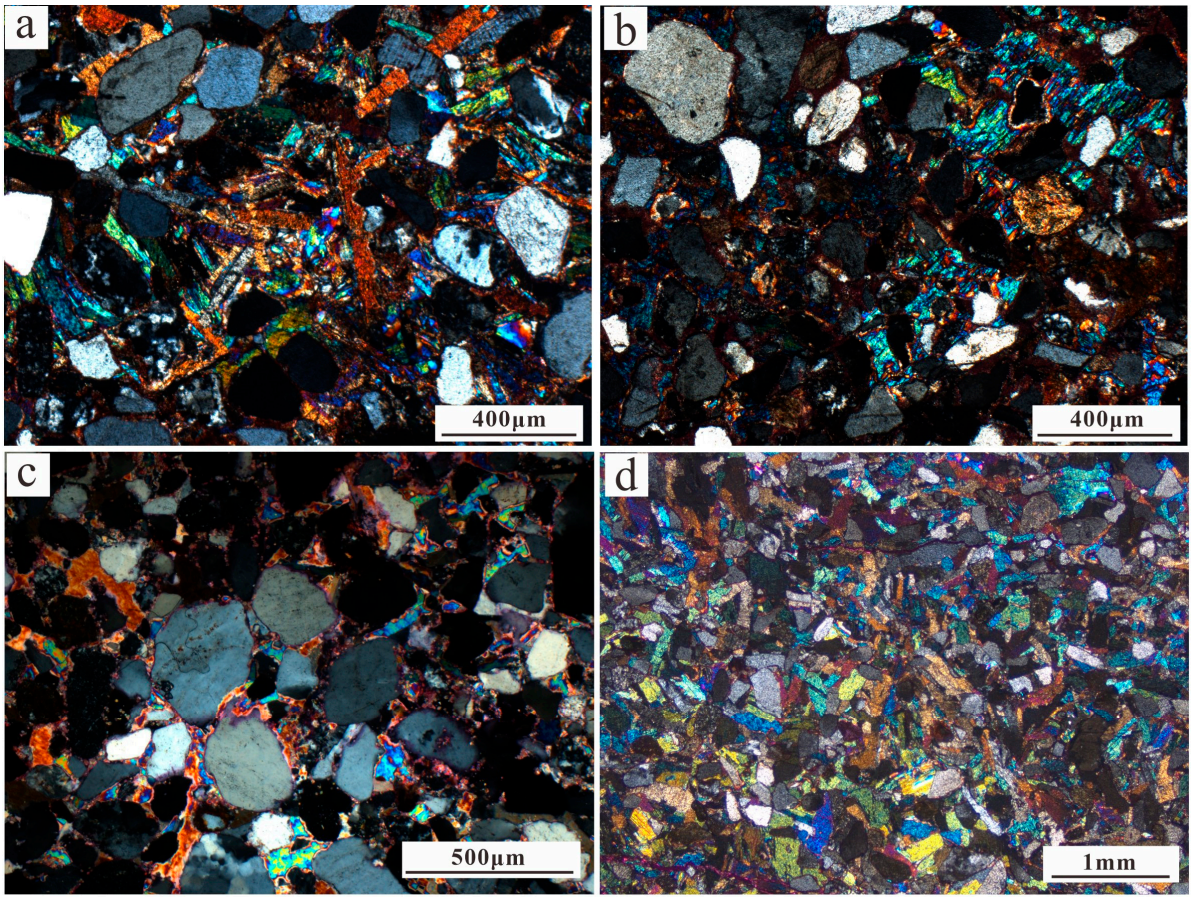


Figure 17. Petrographic features of spotted gypsum observed in thin sections under cross-polarized light. (**a**) PL101, 5659.4 m, gypsum crystals fill the sandstone pores, showing fibrous and prismatic habits; (**b**) PL101, 5657.4 m, gypsum fills the pores as cement, exhibiting interference colors; (**c**) YD101, 4972.3 m, gypsum cement exhibits a banded distribution within pores, mostly showing scaly or microcrystalline mosaic textures; the cement cuts across grain boundaries, forming a typical "invasive" texture; (**d**) PL103, 5616.1 m, gypsum occurs as crystals coexisting with detrital grains, with relatively high crystal content.

The distribution of gypsum nodules is closely associated with the sedimentary structures of the host rocks and the hydrodynamic conditions [95–97]. Random arrangements of nodules (Figure 13f) typically form in environments with complex hydrodynamics, such as shallow waters influenced by rivers or waves. In these areas, the pore structure of detrital sediments becomes irregular after deposition, resulting in a more chaotic distribution of gypsum nodules. Gypsum nodules with oriented distribution mainly develop in environments with relatively stable hydrodynamic conditions. During this period, the pore structures are relatively uniform, which facilitates the enrichment of nucleating fluids along specific bedding planes, promoting the alignment of gypsum nodules in a directional manner (Figure 13c) [93,96,98]. The vertical rhythmicity of gypsum nodules (Figure 13c) is associated with fluctuations in lake levels [99,100]. When the lake level falls, the depositional environment shifts toward relatively higher-energy shallow water areas, resulting in coarser sediment grain sizes, larger and better-connected pore spaces, and increased pore water salinity, which favors the formation of larger gypsum nodules. Conversely, when the lake level rises, depositional energy decreases, sediment grain size becomes finer, and pore space diminishes, restricting fluid movement. Increased freshwater input lowers pore water salinity, limiting crystal growth and resulting in relatively smaller nodules.

Isolated gypsum nodules (Figure 13b,d,e) typically form in environments where local changes in pore structure reduce fluid convection and limit material diffusion [101]. Compaction and cementation during the diagenetic stage further modify the pore structure, restricting material migration and allowing gypsum nodules to grow at specific locations [90,102]. Additionally, late-stage compaction may result in nodules exhibiting irregular angular shapes (Figure 13d).

5.1.5. Mixed Deposition of Clastic Rocks and Gypsum

Gypsiferous mudstone (Figure 14c) and muddy gypsum (Figure 14a) suggest that gypsum primarily formed through in situ precipitation. The associated grayish-green muddy sediments reflect relatively stable, low-energy hydrodynamic conditions that were favorable for gypsum deposition [103]. The sporadic occurrence of muddy clasts within the strata indicates intermittent flood events [45]. Consequently, this lithofacies type typically developed in the transitional zone between the distal delta front and the marginal shallow lacustrine area.

The gypsiferous mudstone containing muddy clasts (Figure 14b) represents short-term, high-energy flood events [59]. The presence of relatively large mud clasts and gypsum fragments indicates a strong hydrodynamic environment. These clasts and fragments originated from eroded gypsum layers and clastic materials in the source area [104] and were transported by floodwaters into the gypsiferous mudstone depositional zone.

The observation of thin sections reveals that in sandy gypsum (Figure 14d), gypsum crystals are intermixed with sandy clastic grains (Figure 16B(d)), showing no significant cementation. This lithofacies also represents flood events, during which rivers eroded unconsolidated gypsum crystals and transported them together with clastic materials to the depositional area [105].

5.2. Control of Seasonal Variations on the Occurrence Characteristics of Gypsum

As previously mentioned, the study area exhibits sedimentary features indicative of seasonal variations under arid climatic conditions, including erosional surfaces composed of brownish-red mud clasts (Figure 3a,c,h) and gypsum debris (Figure 11), dry cracks (Figure 4a,c), interbedded thin layers of gypsum and mudstone (Figures 9c and 7c), horizontal laminations formed by alternating light and dark brownish-red mudstones (Figure 7g), and the interbedding of gray-green and brown-red mudstones (Figure 7c,e). These features collectively reflect the alternation between dry and flood periods [106–108]. Influenced by seasonal variations, the lake area of continental saline basins fluctuates frequently, which simultaneously regulates the input of terrigenous clastic material [109,110]. As a result, the basin exhibits complex sedimentary characteristics marked by the coexistence of clastic rocks and evaporites [111].

Seasonal changes affect the mechanical transport and chemical deposition processes in continental saline lakes, resulting in varying occurrences of gypsum. During the dry period, the supply of terrigenous material decreases or even stops. As evaporation continues, the saline lake water becomes increasingly concentrated, leading to predominantly chemical deposition, forming layered gypsum (Figure 15A, Figure 18A, and Figure 18A(c–e)). Only in the central part of the lake basin, where the water salinity is lower, may mud deposits exist (Figures 15A and 18A). In the delta, the concentration of water also leads to the formation of small, closed, or semi-closed lakes with higher salinity in low-lying areas. The salts in these lakes primarily come from the periodic fluctuations in lake levels, and layered gypsum is also formed during the dry period (Figure 15A, Figure 18A, and Figure 18A(a,b)). When the water body dries up and the gypsum layers are exposed at the surface, they often display cracking due to shrinkage from water loss (Figure 15A(a)). During early

diagenesis, compaction in the burial environment, combined with the continued growth of gypsum crystals, promotes the gradual contact and fusion of crystals, expelling the matrix and forming a network structure (Figure 18A(c–e)). During the dry period, the high-concentration brine in the unconsolidated clastic rock pores continues to evaporate, leading to the precipitation of gypsum in the sediments, which facilitates the growth of gypsum nodules (Figure 18A(c,d)) and spot-like gypsum (Figure 18A(f)). During the flood period, water dynamics are enhanced with the increase in rainfall and river flow, which can destroy and transport the gypsum layers formed earlier (Figure 18B(g–i)). As the transport distance increases and the water dynamics weaken, gypsum clasts may settle in corresponding areas, exhibiting a distribution pattern that evolves from tear-shaped, cloud-like, and conglomeratic-textured to oriented gypsum clasts (Figures 16B and 18B). Mud deposits predominate at the distal part of the delta front, where water dynamics are relatively low (Figure 18B(j)). The occurrence of flood events can transport both terrigenous clasts and unconsolidated gypsum crystals to the deposition area, forming a sedimentary characteristic of the coexistence of clastic rocks and evaporite salts (Figure 14b,d). At the distal part of the delta front, where hydrodynamics are weaker, terrigenous mud deposits and gypsum crystals formed by chemical processes can be deposited together, forming muddy gypsum and gypsiferous mudstone (Figure 14a,c).

5.3. Control of Aridity Intensity Variations on Lithological Distribution

Climate change in the study area is the primary factor controlling the distribution of clastic and evaporitic rocks. Lithologic logging data indicate that during the Early LST stage, gypsum was more extensively distributed, and sandstone bodies were relatively thin (Figure 18C), with gypsum commonly exhibiting a light reddish hue (Figure 18A(d,e),C), suggesting an overall arid climate. During this period, low precipitation and reduced terrigenous input, combined with intense evaporation, promoted widespread gypsum accumulation. Due to limited clastic supply, sandstone bodies were thinner; however, as the lake area gradually shrank, the sand bodies extended over longer lateral distances. During the Late LST stage, the distribution range of gypsum decreased while sandstone bodies became thicker (Figure 18C). The gypsum is predominantly milky white in color (Figure 18B(k)), indicating a relatively humid climate during this period. Increased rainfall and riverine input led to thicker sand bodies and an expansion of the lake basin, with sand bodies gradually retrograding. The influx of freshwater reduced salinity near the delta front, suppressing the formation of nearshore evaporites. In contrast, in areas farther from the delta, salinity remained high, allowing gypsum to continue accumulating, though its distribution was significantly more limited compared with the Early LST. The sedimentary interval represented in Figure 18C records a gradual decline in aridity and reflects an evolution sequence alternately dominated by evaporites and clastic rocks, highlighting a longer-term climatic transition.

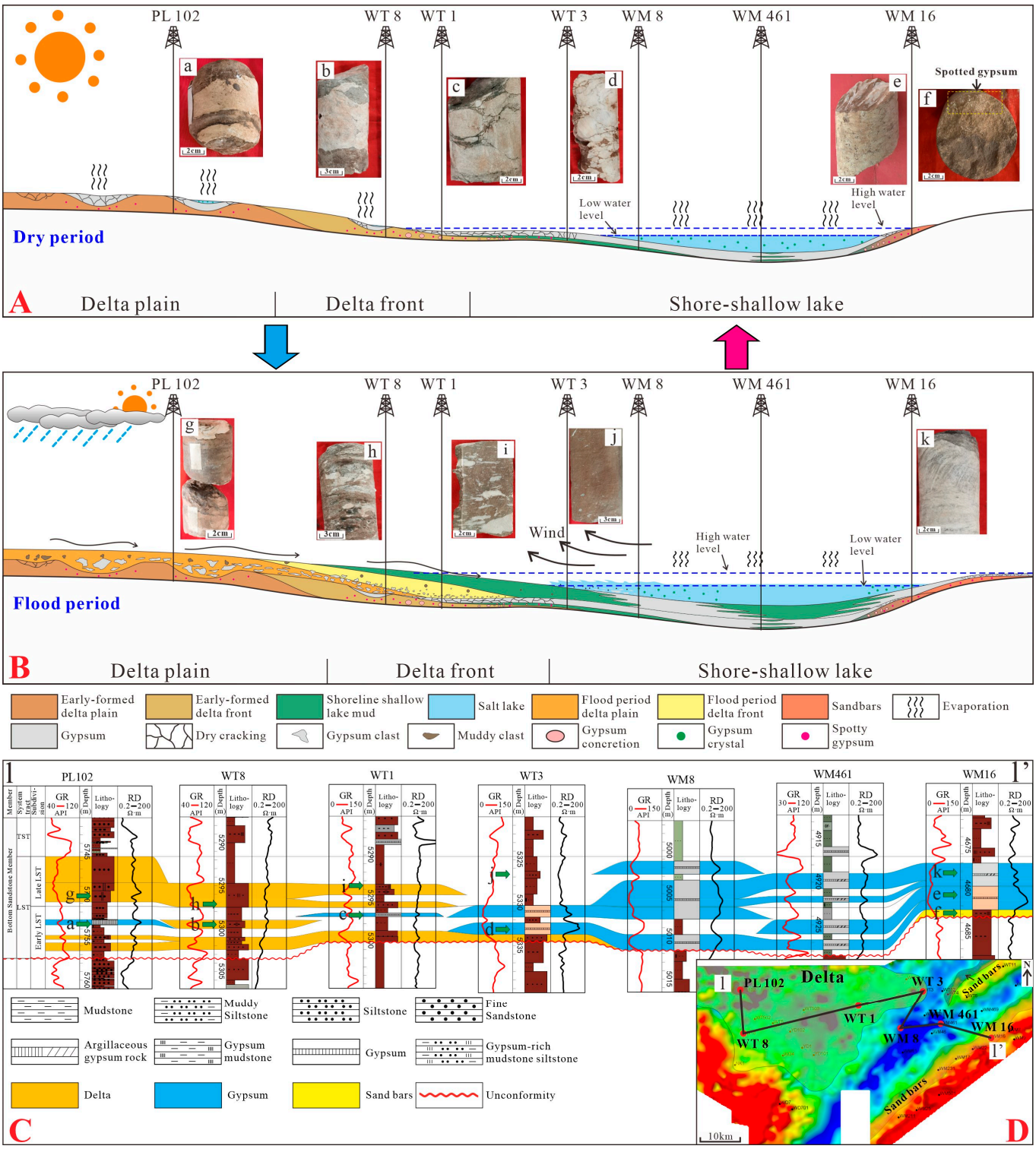


Figure 18. Sedimentary model of the delta–saline lake system under seasonal variations. (**A**) Depositional model during the dry period; (**B**) depositional model during the flood period; (**C**) correlation profile of wells PL102–WM16 (location shown in Figure 18D); (**D**) paleogeomorphology prior to the deposition of the Bottom Sandstone Member, with deltaic deposition in the west and sand bar development near uplifts in the east and northeast. The base map is from the Tarim Oilfield database. The paleogeomorphology location is shown in the blue box in Figure 1C. (**a**) PL102, 5753.5 m, light red layered gypsum; (**b**) WT8, 5299.6 m, milky white layered gypsum; (**c**) WT1, 5297.1 m, milky white network gypsum, showing gypsum nodules; (**d**) WT3, 5333.1 m, light red network gypsum; (**e**) WM16, 4680.8 m, light red network gypsum; (**f**) WM16, 4692.9 m, brown fine sandstone, spotted

gypsum; (**g**) PL102, 5750.1 m, brown fine sandstone, tear-shaped gypsum; (**h**) WT8, 5297.1 m, brown fine sandstone, oriented gypsum, with small mud clasts; (**i**) WT1, 5293.6 m, brown mudstone-siltstone, cloud-like gypsum, oriented gypsum; (**j**) WT3, 5326.7 m, brown mudstone-siltstone, gray-green mud clasts, spotted gypsum; (**k**) WM16, 4678.1 m, milky white gypsum. l–l′ marks the cross-section location in Figure C.

6. Conclusions

This study integrated core, thin-section, and logging data to analyze the sedimentary environment and development of gypsum in the western Tabei Uplift, focusing on the genesis of gypsum and the influence of seasonal variations on its occurrence.

(1) The western part of the Tabei Uplift developed a salt lake–delta sedimentary system under the influence of the Tethys Ocean transgression and persistent arid conditions.
(2) Five types of gypsum occurrence are identified in the study area: layered gypsum, gypsum clasts, spotty gypsum, gypsum nodules, and a mixed deposition of clastic rocks and gypsum. These can be grouped into two genetic categories: in situ precipitation and allochthonous transport. In situ gypsum forms via chemical precipitation during evaporation. Gypsum formed through allochthonous transportation is primarily in the form of gypsum clasts. As the transport distance increases, gypsum exhibits an evolutionary sequence from tear-shaped, cloud-like, and conglomeratic-textured to flat-elliptical gypsum.
(3) Seasonal variations control the development characteristics of gypsum. During the dry period, gypsum primarily forms through chemical precipitation. Evaporation in the saline lake leads to the formation of layered gypsum deposits, while gypsum precipitated from the pore water of clastic sediments can form spotty and nodular gypsum. During flood periods, enhanced surface runoff transports terrigenous clastic material into the lake, leading to a decrease in water salinity. Stronger hydrodynamics during the flood period erode previously formed gypsum layers, transporting and depositing them together with clastic materials.

Author Contributions: Conceptualization, X.G. and L.D.; methodology, X.G. and L.D.; validation, Q.S.; formal analysis, B.L.; investigation, W.H.; resources, Z.Y.; data curation, Q.S.; writing—original draft preparation, X.G.; writing—review and editing, X.G., W.H., and L.D.; visualization, J.Y.; supervision, B.L.; project administration, Z.Y.; funding acquisition, W.H. All authors have read and agreed to the published version of the manuscript.

Funding: This research was supported by the National Natural Science Foundation of China (Grant No. 42202177).

Data Availability Statement: Data are contained within the article.

Conflicts of Interest: All authors with commercial affiliations are listed as follows: Jingwen Yan, Qi Sun, Zhenli Yi, and Bin Li are employed by Tarim Oilfield Company. All other authors declare no commercial or financial conflicts of interest related to this research.

References

1. Omidpour, A.; Rahimpour-Bonab, H.; Moussavi-Harami, R.; Mahboubi, A. Anhydrite fabrics as an indicator for relative sea-level signatures in the sequence stratigraphic framework of a carbonate ramp. *Mar. Pet. Geol.* **2023**, *155*, 106400. [CrossRef]
2. Zhang, X.; Gao, Z.; Maselli, V.; Fan, T. Tectono-sedimentary characteristics and controlling factors of the lower-middle Cambrian gypsum-salt rocks in the Tarim Basin, Northwest China. *Mar. Pet. Geol.* **2023**, *151*, 106189. [CrossRef]
3. Buck, B.J.; Van Hoesen, J.G. Assessing the applicability of isotopic analysis of pedogenic gypsum as a paleoclimate indicator, Southern New Mexico. *J. Arid Environ.* **2005**, *60*, 99–114. [CrossRef]
4. Kasprzyk, A. Sedimentological and diagenetic patterns of anhydrite deposits in the Badenian evaporite basin of the Carpathian Foredeep, southern Poland. *Sediment. Geol.* **2003**, *158*, 167–194. [CrossRef]

5. Aleali, M.; Rahimpour-Bonab, H.; Moussavi-Harami, R.; Jahani, D. Environmental and sequence stratigraphic implications of anhydrite textures: A case Omidpour from the Lower Triassic of the Central Persian Gulf. *J. Asian Earth Sci.* **2013**, *75*, 110–125. [CrossRef]
6. Makhnach, A.; Shimanovich, V.; Streltsova, G.; Mikhajlov, N. Anhydrite and gypsum in the Devonian and Permian evaporite lithofacies of Belarus: A review. *Geol. Q.* **2014**, *3*, 58. [CrossRef]
7. Yeşilova, G.P.; Gökmen, D. The paleodepositional environment, diagenetic and depositional conditions of the Middle-Late Miocene Koluz gypsum member (NE Van, Eastern Turkey). *Carbonates Evaporites* **2020**, *35*, 76. [CrossRef]
8. Liu, T.; Jiang, Z.; Jia, H.; Wu, X.; Yu, J.; Zhao, B.; Wei, S. Controlling factors of the gypsum-salt strata differences within two adjacent Eocene sags in the eastern Jiyang Depression, NE China and its hydrocarbon significance. *Geoenergy Sci. Eng.* **2023**, *231*, 212352. [CrossRef]
9. Bain, R.J. Diagenetic, nonevaporative origin for gypsum. *Geology* **1990**, *18*, 447–450. [CrossRef]
10. Warren, J.K. Evaporites through time: Tectonic, climatic and eustatic controls in marine and nonmarine deposits. *Earth-Sci. Rev.* **2010**, *98*, 217–268. [CrossRef]
11. Murray, R.C. Origin and diagenesis of gypsum and anhydrite. *J. Sediment. Res.* **1964**, *34*, 512–523.
12. Ortí, F.; Rosell, L.; Anadón, P. Diagenetic gypsum related to sulfur deposits in evaporites (Libros Gypsum, Miocene, NE Spain). *Sediment. Geol.* **2010**, *228*, 304–318. [CrossRef]
13. Tang, M.; Ehreiser, A.; Li, Y.L. Gypsum in modern Kamchatka volcanic hot springs and the Lower Cambrian black shale: Applied to the microbial-mediated precipitation of sulfates on Mars. *Am. Mineral.* **2014**, *99*, 2126–2137. [CrossRef]
14. Babel, M. Models for evaporite, selenite and gypsum microbialite deposition in ancient saline basins. *Acta Geol. Pol.* **2004**, *54*, 219–249.
15. Allwood, A.C.; Burch, I.W.; Rouchy, J.M.; Coleman, M. Morphological Biosignatures in Gypsum: Diverse Formation Processes of Messinian (∼6.0 Ma) Gypsum Stromatolites. *Astrobiology* **2013**, *13*, 870–886. [CrossRef]
16. Buck, B.J.; Van Hoesen, J.G. Snowball morphology and SEM analysis of pedogenic gypsum, southern New Mexico, U.S.A. *J. Arid Environ.* **2002**, *51*, 469–487. [CrossRef]
17. Taimeh, A.Y. Formation of Gypsic Horizons in Some Arid Regions Soils of Jordan. *Soil Sci.* **1992**, *153*, 486–498. [CrossRef]
18. Olson, K.J.; Demicco, R.V.; Lowenstein, T.K. Seasonal dynamics of evaporite mineral precipitation, dissolution, and back-reactions in shallow and deep hypersaline lakes. *Geochim. Cosmochim. Acta* **2023**, *351*, 51–65. [CrossRef]
19. Westerhold, T.; Marwan, N.; Drury, A.J.; Liebrand, D.; Agnini, C.; Anagnostou, E.; Barnet, J.S.; Bohaty, S.M.; De Vleeschouwer, D.; Florindo, F.; et al. An astronomically dated record of Earth's climate and its predictability over the last 66 million years. *Science* **2020**, *36*, 1383–1387. [CrossRef]
20. O'Brien, C.L.; Robinson, S.A.; Pancost, R.D.; Damsté, S.J.S.; Schouten, S.; Lunt, D.J.; Alsenz, H.; Bornemann, A.; Bottini, C.; Brassell, S.C.; et al. Cretaceous sea-surface temperature evolution: Constraints from TEX86 and planktonic foraminiferal oxygen isotopes. *Earth-Sci. Rev.* **2017**, *172*, 224–247. [CrossRef]
21. Zachos, J.; Dickens, G.; Zeebe, R. An early Cenozoic perspective on greenhouse warming and carbon-cycle dynamics. *Nature* **2008**, *451*, 279–283. [CrossRef] [PubMed]
22. Zhang, S.; Hu, X.; Han, Z.; Li, J.; Garzanti, E. Climatic and tectonic controls on Cretaceous-Palaeogene sea-level changes recorded in the Tarim epicontinental sea. *Palaeogeogr. Palaeoclimatol. Palaeoecol.* **2018**, *501*, 92–110.
23. Yue, Y.; Jiang, S.; Tian, J.; Lin, X. Late Cretaceous to Early Paleocene sedimentary environment evolution: Geochemical evidences of Well PBX1 in the southwestern Tarim Basin. *Geol. China* **2024**, *51*, 592–605.
24. Kaya, M.Y.; Dupont-Nivet, G.; Proust, J.N.; Bougeois, L.; Meijer, N.; Frieling, J.; Fioroni, C.; Roperch, P.; Mamtimin, M.; Aminov, J.; et al. The Cretaceous–Paleogene paleogeography of Central Asia recorded in depositional environments of the Proto-Paratethys Sea in the Tarim Basin (Western China). *Eur. Geosci. Union Gen. Assem.* **2017**, *19*, EGU2017-9973.
25. Zhang, Z.; Lin, C.; Liu, Y.; Liu, J.; Zhou, H.; Li, H.; Sun, Q.; Xia, H.; Ma, M.; Liang, Y. Lacustrine to fluvial depositional systems: The depositional evolution of an intracontinental depression and controlling factors, Lower Cretaceous, northern Tarim Basin, northwest China. *Mar. Pet. Geol.* **2021**, *126*, 104904.
26. Yang, Y.; Tian, J.; Zhang, X.; Li, Y.; Zhang, Y.; Xia, Q. Characteristics and Geological Significance of High-Frequency Cycles in Salinized Lake Basins: The Paleogene Kumugeliemu Group in the Xinhe Area, Northern Tarim Basin. *Minerals* **2023**, *13*, 824. [CrossRef]
27. Kordi, M. Sedimentary basin analysis of the Neo-Tethys and its hydrocarbon systems in the southern Zagros fold-thrust belt and foreland basin. *Earth-Sci. Rev.* **2019**, *19l*, 1–11.
28. Xi, D.; Tang, Z.; Wang, X.; Qin, Z.; Cao, W.; Jiang, T.; Wu, B.; Li, Y.; Zhang, Y.; Jiang, W.; et al. The Cretaceous- Paleogene marine stratigraphic framework that records significant geological events in the western Tarim Basin. *Earth Sci. Front.* **2020**, *27*, 165–198.
29. Xu, Y.; Cao, Y.; Liu, C. Brine Temperature of Early Eocene Salt Formation Period in Kuqa Basin and Its Significance. *Earth Sci.* **2021**, *46*, 4188–4196.

30. Chen, L.; Lin, C.; Li, H.; Xiang, S. Sedimentary characteristics of the lower sandstone part of Kumugeliemu group in the western Tabei uplift. *J. Northeast Pet. Univ.* **2017**, *41*, 23–32.
31. Liu, J.; Lin, C.; Lai, X.; Yang, Y.; Yang, X.; Si, B. Depositional paleogeography and source rock analysis of the lower sandstone part of Eogene Kumugeliemu Group in Kuga depression. *Acta Petrol. Mineral.* **2008**, *27*, 538–546.
32. Wang, Q.; Xu, Z.; Zhang, R.; Yang, H.; Yang, X. New fields, new types of hydrocarbon explorations and their resource potentials in Tarim Basin. *Acta Pet. Sin.* **2024**, *45*, 15–32.
33. Huang, S.; Yang, W.; Lu, Y.; Zhang, K.; Zhao, Q.; Fan, S. Geological conditions, resource potential and exploration direction of natural gas in Tarim Basin. *Nat. Gas Geosci.* **2018**, *29*, 1497–1505.
34. An, H.; Li, H.; Wang, J.; Du, X. Tectonic Evolution and lts Controlling on Oil and Gas Accumulation in the Northern Tarim Basin. *Geotecton. Metallog.* **2009**, *33*, 142–147.
35. Xu, G.; Liu, S.; Li, G.; Wu, H.; Yan, X. Comparison of tectonic evolutions and petroleum geological conditions in Tazhong and Tabei palaeohighs in Tarim Basin. *Oil Gas Geol.* **2005**, *26*, 114–119.
36. Wu, G.; Li, Q.; Xiao, Z.; Li, H.; Zhang, L.; Zhang, X. The Evolution Characteristics of Palaeo-Uplifts in Tarim Basin and lts Exploration Directions for Oil and Gas. *Geotecton. Metallog.* **2009**, *33*, 124–130.
37. Liu, C. Geochemistry Characteristic and Origin of Paleogene Dolomite in Kuqa Depression, Tarim Basin. *Acta Sedimentol. Sin.* **2010**, *28*, 518–524.
38. Cao, Y. Marine transgressive–regressive cycles and evolution on ancient salt lake in the northwestern Tarim Basin in the Paleocene, Xinjiang Province, China. *Carbonates Evaporites* **2022**, *37*, 21. [CrossRef]
39. Zhao, X.; Gao, Z.; Feng, J.; Li, X.; Guo, M. Triassic-Neogene Heavy Minerals' Assemblages Characteristics and Basin-Orogen Tectonic Evolution Relationship in the Kuqa Foreland Basin. *Acta Sedimentol. Sin.* **2014**, *32*, 68–77.
40. Wu, J.; Zhu, C.; Yang, G.; Zhang, J.; Gong, Q.; Song, Y. High-resolution sequence stratigraphy characteristics and sedimentary facies evolution of thin sands under high-frequency lake level change: A case study of lower sand Member of Paleogene Kumugeliemu Group in margin of Wensu Uplift-Yingmaili Uplift area. *Pet. Geol. Recovery Effic.* **2020**, *27*, 38–46.
41. Miall, A.D. Architectural elements and bounding surfaces in fluvial deposits: Anatomy of the Kayenta Formation (lower Jurassic), Southwest Colorado. *Sediment. Geol.* **1988**, *55*, 233–262. [CrossRef]
42. Andrews, P.B. Deltaic sediments, Upper Triassic Torlesse Supergroup, Broken River, North Canterbury. *N. Zeal. J. Geol. Geophys.* **1974**, *17*, 881–905. [CrossRef]
43. Strohmenger, C.J.; Al-Mansoori, A.; Al-Jeelani, O.; Al-Shamry, A.; Al-Hosani, I.; Al-Mehsin, K.; Shebl, H. The sabkha sequence at Mussafah Channel (Abu Dhabi, United Arab Emirates): Facies stacking patterns, microbial-mediated dolomite and evaporite overprint. *GeoArabia* **2010**, *15*, 49–90. [CrossRef]
44. Mary, J.; Stephen, K.; Hasiotis, T. Significance of Different Modes of Rhizolith Preservation to Interpreting Paleoenvironmental and Paleohydrologic Settings: Examples from Paleogene Paleosols, Bighorn Basin, Wyoming, U.S.A. *J. Sediment. Res.* **2006**, *76*, 633–646.
45. Mahmoud, A.M.A. Classification and depositional environments of Quaternary pedogenic gypsum crusts (gypcrete) from east of the Fayum Depression, Egypt. *Sediment. Geol.* **2003**, *155*, 87–108.
46. Jopling, A.V. Hydraulic studies on the origin of bedding. *Sedimentology* **1963**, *2*, 115–121. [CrossRef]
47. Jain, S. *Fundamentals of Sedimentology*; CRC Press: Boca Raton, FL, USA, 2024.
48. Wang, J.; Hu, Z.; Li, S.; Cai, Q.; Guo, Y.; Zuo, Y.; Pang, Y. Distribution characteristics and sedimentary model of gypsum-bearing evaporite of the Middle Cambrian Gaotai Formation in the eastern Sichuan Basin. *Arab. J. Geosci.* **2022**, *15*, 1056. [CrossRef]
49. Cai, Q.; Hu, M.; Liu, Y.; Kane, O.; Deng, Q.; Hu, Z.; Li, H.; Ngia, N. Sedimentary characteristics and implications for hydrocarbon exploration in a retrograding shallow-water delta: An example from the fourth Member of the Cretaceous Quantou Formation in the Sanzhao depression, Songliao Basin, NE China. *Pet. Sci.* **2022**, *19*, 929–948. [CrossRef]
50. Fan, Q.; Fan, T.L.; Li, Q.P.; Du, Y.; Zhang, Y.; Yuan, Y. Sedimentary characteristics and development model of Cambrian gypsum-salt rocks in Tarim Basin. *Pet. Geol. Exp.* **2021**, *43*, 217–226.
51. Brian, G.J.; Brian, R.R. Massive sandstone facies in the Hawkesbury Sandstone, a Triassic fluvial deposit near Sydney, Australia. *J. Sediment. Res.* **1983**, *53*, 1249–1259.
52. Alonso-Zarza, A.M.; Zhao, Z.; Song, C.H.; Li, J.J.; Zhang, J.; Martín-Pérez, A.; Martín-García, R.; Wang, X.X.; Zhang, Y.; Zhang, M.H. Mudflat/distal fan and shallow lake sedimentation (upper Vallesian–Turolian) in the Tianshui Basin, Central China: Evidence against the late Miocene eolian loess. *Sediment. Geol.* **2009**, *222*, 42–51. [CrossRef]
53. Dolores, A.V.D.K.; Peter, P.F.; Stephen, T.H. Paleoenvironmental Reconstruction of A Late Cretaceous, Muddy, River-Dominated Polar Deltaic System: Schrader Bluff–Prince Creek Formation Transition, Shivugak Bluffs, North Slope of Alaska, U.S.A. *J. Sediment. Res.* **2015**, *85*, 903–936.
54. Allen, J.R.L. A review of the origin and characteristics of recent alluvial sediments. *Sedimentology* **1965**, *5*, 89–191.

55. Buatois, L.A.; Santiago, N.; Herrera, M.; Plink-Björklund, P.; Steel, R.; Espin, M.; Parra, K. Sedimentological and ichnological signatures of changes in wave, river and tidal influence along a Neogene tropical deltaic shoreline. *Sedimentology* **2012**, *59*, 1568–1612. [CrossRef]
56. Greenwood, B. Bimodal Cross-Lamination in Wave-Ripple Form Sets: A Possible Origin. *J. Coast. Res.* **2006**, *225*, 1220–1229.
57. Niu, T.; Hu, G.; Fan, T.; Wang, H.; Hu, X. The Mixed Clastic-Carbonate Sedimentation Model in Shujiutuo Area, Bohai Bay Basin. *Adv. Geosci.* **2019**, *9*, 9. [CrossRef]
58. Mu, C.; Zhou, H.; Chen, A.; Hou, M. Mixed siliciclastic—Carbonate: Progress and new idea of classification. *Acta Sedimentol. Sin.* **2025**, 1–17. [CrossRef]
59. Zhang, L.; Bao, Z.D.; Dou, L.; Zang, D.; Mao, D.; Song, J.; Zhao, J.; Wang, Z. Sedimentary characteristics and pattern of distributary channels in shallow water deltaic red bed succession: A case from the Late Cretaceous Yaojia Formation, southern Songliao Basin, NE China. *J. Pet. Sci. Eng.* **2018**, *171*, 1171–1190.
60. Gugliotta, M.; Flint, S.S.; Hodgson, D.M.; Veiga, G.D. Stratigraphic Record of River-Dominated Crevasse Subdeltas with Tidal Influence (Lajas Formation, Argentina). *J. Sediment. Res.* **2015**, *85*, 265–284. [CrossRef]
61. Yannick, C.; André, L. The transformation of ferrihydrite into goethite or hematite, revisited. *J. Solid State Chem.* **2006**, *179*, 716–722.
62. Zhang, L.; Bao, Z.; Lin, Y.; Chen, Y.; Lin, X.; Dou, L.; Kong, B. Genetic types and sedimentary model of sandbodies in a shallow-water delta: A case study of the first Member of Cretaceous Yaojia Formation in Qian'an area, south of Songliao Basin, NE China. *Pet. Explor. Dev.* **2017**, *44*, 770–779. [CrossRef]
63. Deng, Q.; Hu, M.; Wu, Y.; Huang, M.; Lu, K.; Cai, Q. Lacustrine to deltaic depositional systems: Sedimentary evolution and controlling factors of an Upper Cretaceous continental depression and implications for petroleum exploration. *Mar. Pet. Geol.* **2025**, *173*, 107234. [CrossRef]
64. Weinberger, R. Initiation and growth of cracks during desiccation of stratified muddy sediments. *J. Struct. Geol.* **1999**, *21*, 379–386. [CrossRef]
65. Wei, Z.; Li, S.; Zhang, T.; Liu, Y.; Yao, Z.; Xu, W.; Li, H. The delta-fluvial evolution of a lacustrine basin with gentle slope and low sedimentation rate: A case study of the Fudong Slope, Junggar Basin, Northwest China. *Sediment. Geol.* **2023**, *453*, 106441. [CrossRef]
66. Niu, X.; Yang, T.; Cao, Y.; Li, S.; Zhou, X.; Xi, K.; Dodd, T.J.H. Characteristics and formation mechanisms of gravity-flow deposits in a lacustrine depression basin: Examples from the Late Triassic Chang 7 oil member of the Yanchang Formation, Ordos Basin, Central China. *Mar. Pet. Geol.* **2023**, *148*, 106048. [CrossRef]
67. Miall, A.D. *The Geology of Fluvial Deposits*; Springer: Berlin, Germany, 1996.
68. Soma, B.; Luca, C.; Mountney, N.P. Quantitative characterization of the sedimentary architecture of Gilbert-type deltas. *Sediment. Geol.* **2021**, *426*, 106022.
69. Li, Y.; Bhattacharya, J. Facies architecture of asymmetrical branching distributary channels: Cretaceous Ferron Sandstone, Utah, USA. *Sedimentology* **2014**, *61*, 1452–1483. [CrossRef]
70. Wu, W.; Liu, J.; Liu, C.; Feng, Z.; Niu, Y.; Wang, G.; Liu, H.; Liu, W.; Liu, J. Sedimentary and ichonology characteristics of continental shelf-edge delta of Zhuiang Formation in Baiyun Sag, Pearl River Mouth Basin. *J. China Univ. Pet. (Ed. Nat. Sci.)* **2020**, *44*, 152–162.
71. Tesi, T.; Miserocchi, S.; Goñi, M.A.; Turchetto, M.; Langone, L.; Lazzari, A.D.; Albertazzi, S.; Correggiari, A. Influence of distributary channels on sediment and organic matter supply in event-dominated coastal margins: The Po prodelta as a study case. *Biogeosciences* **2011**, *8*, 365–385. [CrossRef]
72. Cappelle, M.V.; Ravnås, R.; Hampson, G.J.; Johnson, H.D. Depositional evolution of a progradational to aggradational, mixed-influenced deltaic succession: Jurassic Tofte and Ile Formations, southern Halten Terrace, offshore Norway. *Mar. Pet. Geol.* **2017**, *80*, 1–22. [CrossRef]
73. Edmonds, D.A.; Slingerland, R.L. Mechanics of river mouth bar formation: Implications for the morphodynamics of delta distributary networks. *J. Geophys. Res. Earth Surf.* **2007**, *112*. [CrossRef]
74. Ponce, J.J.; Carmona, N.; Jait, D.; Cevallos, M.; Rojas, C. Sedimentological and ichnological characterization of delta front mouth bars in a river-dominated delta (Upper Cretaceous) from the La Anita Formation, Austral Basin. Argentina. *Sedimentology* **2024**, *71*, 27–53. [CrossRef]
75. Van, Y.A.E.; Poyatos-Moré, M.; Holbrook, J.M.; Midtkandal, I. Internal mouth-bar variability and preservation of subordinate coastal processes in low-accommodation proximal deltaic settings (Cretaceous Dakota Group, New Mexico, USA). *Depos. Rec.* **2020**, *6*, 431–458.
76. Xi, D.; Wan, X.; Jansa, L.; Zhang, Y. Late Cretaceous paleoenvironment and lake level fluctuation in the Songliao Basin, northeastern China. *Isl. Arc* **2015**, *20*, 6–22. [CrossRef]
77. Li, S.; Li, S.; Shan, X.; Gong, C.; Yu, X. Classification, formation, and transport mechanisms of mud clasts. *Int. Geol. Rev.* **2017**, *59*, 1609–1620. [CrossRef]

78. Lei, C.; Song, X.; Gao, X.; Wang, R.; Zhai, G.; Xu, Q.; Feng, W.; Yin, Y. Formation process and internal architecture of wave dominated beach-bar along the lake shore: Insights from a flume experiment. *Arab. J. Geosci.* **2021**, *14*, 2043. [CrossRef]
79. Liu, Y.; Luo, J.; Huang, H.; Peng, W.; Liu, Z.; Chen, J. Beach bar genesis of the lower member of Xingouzui Formation in the southern slope zone of Jiangling sag, Jianghan Basin, and its controlling factors. *China Pet. Explor.* **2016**, *21*, 92–98.
80. Zhang, C.; Han, J.; Ji, Y.; Zhou, Y.; Su, R.; Wang, S.; Yin, J.; Zhang, S.; Tang, L.; Liu, J. Distribution characteristics and stacking patterns of sandbodies in the continental lacustrine fan delta-beach dam system: A case study from submember 3 upper of Paleogene Shahejie Formation in Liuxi area, Raoyang Sag, Bohai Bay Basin. *Nat. Gas Geosci.* **2020**, *31*, 518–531.
81. Bruckner, W.D. Cyclic Calcareous Sedimentation as an Index of Climatic Variations in the Past. *SEPM J. Sediment. Res.* **1953**, *23*, 235–237.
82. Zhang, H.; Liu, C.; Cao, Y.; Sun, H.; Wang, L. A Tentative Discussion on the Time and the Way of Marine Regression from Tarim Bay during the Cenozoic. *Acta Geosci. Sin.* **2013**, *34*, 577–584.
83. Luo, L.; Guo, J.; Hu, C.; Lin, H.; Quaye, J.A.; Zhou, X.; Han, B. Sedimentary characteristics and development model of the bedded evaporites in the Paleogene Kumugeliemu formation, Kuqa depression, Northwestern China. *Carbonates Evaporites* **2024**, *39*, 68. [CrossRef]
84. Zhou, X.; Lin, H.; Guo, J.; Yao, W.; Zhang, T.; Zhou, X.; Luo, L. Depositional model and petroleum significance of the Cretaceous Yageliemu Formation in Xinhe area on the southern slope of Kuqa Depression, Tarim Basin. *Pet. Geol. Exp.* **2023**, *45*, 266–279.
85. Hardie, L.A.; Smoot, J.P.; Eugster, H.P. Saline Lakes and their Deposits: A Sedimentological Approach. In *Modern & Ancient Lake Sediments*; John Wiley & Sons: Hoboken, NJ, USA, 1978; pp. 7–41.
86. Mohammadi, A.; Lak, R.; Schwamborn, G.; Firouz, A.K.; Çiner, A.; Khatouni, J.D. Depositional Environments and Salt-thickness Variations in Urmia Lake (NW IRAN): Insight from Sediment-core Studies. *J. Sediment. Res.* **2021**, *91*, 296–316. [CrossRef]
87. Warren, J.K.; Kendall, C.G.S.T.C. Comparison of Sequences Formed in Marine Sabkha (Subaerial) and Salina (Subaqueous) Settings—Modern and Ancient. *AAPG Bull.* **1985**, *69*, 1013–1023.
88. Hardie, L.A.; Eugster, H.P. The depositional environment of marine evaporites: A case for shallow, clastic accumulation. *Sedimentology* **2010**, *16*, 187–220. [CrossRef]
89. Baria, L.R. Desiccation features and the reconstruction of paleosalinities. *J. Sediment. Res.* **1977**, *47*, 908–914.
90. Kadkhodaie, R.; Sohrabi, A.; Jodeyri-Agaii, R. A syngenetic classification of anhydrite textures in carbonate reservoirs and its relationship with reservoir quality: A case study from the Permo-Triassic Dalan and Kangan formations. *Carbonates Evaporites* **2022**, *37*, 44. [CrossRef]
91. Hussain, M.; Warren, J.K. Nodular and enterolithic gypsum: The "sabkha-tization" of Salt Flat playa, west Texas. *Sediment. Geol.* **1989**, *64*, 13–24. [CrossRef]
92. Elorza, M.G.; Santolalla, F.G. Geomorphology of the Tertiary gypsum formations in the Ebro Depression (Spain). *Geoderma* **1998**, *87*, 1–29. [CrossRef]
93. Deng, W.; Tan, X.; Zhang, D.; Zhong, S. Occurrence types and genesis of anhydrite from the Ma5 submember of Ordovician Majiagou Formation in central and eastern Ordos Basin. *J. Palaeogeogr. (Chin. Ed.)* **2022**, *24*, 226–244.
94. Machel, H.G.; Burton, E.A. Burial-diagenetic sabkha-like gypsum and anhydrite nodules. *J. Sediment. Res.* **1991**, *61*, 394–405.
95. Warren, J.K. *Evaporites: Sediments, Resources and Hydrocarbons*; Springer Science & Business Media: Berlin/Heidelberg, Germany, 2006.
96. Smoot, J.P.; Lowenstein, T.K. Depositional environments of non-marine evaporites. In *Developments in Sedimentology*; Melvin, J.L., Ed.; Elsevier: Amsterdam, The Netherlands, 1991; Volume 50, pp. 189–347.
97. Sanz-Rubio, E.; Hoyos, M.; Calvo, J.P.; Rouchy, J.M. Nodular anhydrite growth controlled by pedogenic structures in evaporite lake formations. *Sediment. Geol.* **1999**, *125*, 195–203. [CrossRef]
98. Hu, G.; Li, G.; Wei, X.; Li, Y. Lithofacies Paleogeography Research on Ordovician Majiagou 5_4 Sub-member in the West Jingbian Platform. *Acta Sedimentol. Sin.* **2017**, *35*, 527–539.
99. Warren, J.K. The hydrological setting, occurrence and significance of gypsum in late Quaternary salt lakes in South Australia. *Sedimentology* **1982**, *29*, 609–637. [CrossRef]
100. Sera1, A.S.B.; Alzughoul, K.A. The Depositional Environment: Diagenetic and Depositional Settings of Gypsum Deposits from Bi'r El Ghanem, NW Libya. *J. Geol. Geophys.* **2021**, *10*, 2455–6211.
101. Ooi, D.S.M. *Origin and Early Diagenesis of Evaporites in a Coastal Sab-Kha*; University of Bristol: Bristol, UK, 2019.
102. Calvo, J.P.; Jones, B.F.; Bustillo, M.; Fort, R.; Alonso Zarza, A.M.; Kendall, C. Sedimentology and geochemistry of carbonates from lacustrine sequences in the Madrid Basin, central Spain. *Chem. Geol.* **1995**, *123*, 173–191. [CrossRef]
103. Maestro, E. Sedimentary evolution of the Late Eocene Vernet lacustrine system (South-Central Pyrenees). Tectono-climatic control in an alluvial-lacustrine piggyback basin. *J. Paleolimnol.* **2008**, *40*, 1053–1078. [CrossRef]
104. Vai, G.B.; Lucchi, F.R. Algal crusts, autochthonous and clastic gypsum in a cannibalistic evaporite basin: A case history from the Messinian of Northern Apennines. *Sedimentology* **1977**, *24*, 211–244. [CrossRef]

105. Mees, F.; Casteñeda, C.; Herrero, J.; Ranst, E.V. The Nature and Significance of Variations In Gypsum Crystal Morphology In Dry Lake Basins. *J. Sediment. Res.* **2012**, *82*, 37–52. [CrossRef]
106. Valero-Garcés, B.L.; Kelts, K.R. A sedimentary facies model for perennial and meromictic saline lakes: Holocene Medicine Lake Basin, South Dakota, USA. *J. Paleolimnol.* **1995**, *14*, 123–149. [CrossRef]
107. Burne, R.V.; Ferguson, J. Contrasting marginal sediments of a seasonally flooded saline lake—Lake Eliza, South Australia: Significance for oil shale genesis. *BMR J. Aust. Geol. Geophys.* **1983**, *8*, 99–108.
108. Benison, K.C.; Goldstein, R.H. Evaporites and siliciclastics of the Permian Nippewalla Group of Kansas, USA: A case for non-marine deposition in saline lakes and saline pans. *Sedimentology* **2001**, *48*, 165–188. [CrossRef]
109. Zou, C.; Zhang, X.; Luo, P.; Wang, L.; Luo, Z.; Liu, L. Shallow-lacustrine sand-rich deltaic depositional cycles and sequence stratigraphy of the Upper Triassic Yanchang Formation, Ordos Basin, China. *Basin Res.* **2010**, *22*, 108–125.
110. Marcello, G.; Colleen, E.K.; Robert, W.D.; Stephen, S.F.; David, M.H. Decoupling seasonal fluctuations in fluvial discharge from the tidal signature in ancient deltaic deposits: An example from the Neuquén Basin, Argentina. *J. Geol. Soc.* **2015**, *173*, 94–107.
111. Flemming, B.W. Langebaan lagoon: A mixed carbonate-siliciclastic tidal environment in a semi-arid climate. *Sediment. Geol.* **1977**, *18*, 61–95. [CrossRef]

Disclaimer/Publisher's Note: The statements, opinions and data contained in all publications are solely those of the individual author(s) and contributor(s) and not of MDPI and/or the editor(s). MDPI and/or the editor(s) disclaim responsibility for any injury to people or property resulting from any ideas, methods, instructions or products referred to in the content.